



1 **Exploring implications of input parameter uncertainties on GLOF modelling**
2 **results using the state-of-the-art modelling code, r.avaflow**

3 **Sonam Rinzin¹, Stuart Dunning¹, Rachel Joanne Carr¹, Ashim Sattar², Martin Mergili³**

4 **¹School of Geography, Politics and Sociology, Newcastle University, United Kingdom**

5 **²Divecha Centre for Climate Change, Indian Institute of Science, India**

6 **³Institute of Geography and Regional Science, University of Graz, Austria**

7 Correspondence to: Sonam Rinzin at s.rinzin2@newcastle.ac.uk

8 **Abstract**

9 Modelling complex mass flow processes like glacial lake outburst floods (GLOFs) for hazard
10 and risk assessments involves substantial data and computational resources, often leading
11 researchers to use low-resolution, open-access data and parameters based on plausibility
12 rather than direct measurement, which, although effective in back analysis, introduces
13 significant uncertainties in forward modelling. To determine the sensitivity of the model outputs
14 stemming from input parameter uncertainties in the forward modelling, we selected nine
15 parameters relevant to GLOF modelling and performed a total of 78 simulations in the
16 physically-based r.avaflow model. Our results indicate that GLOF modelling outputs are
17 notably sensitive to six parameters, which are, in order of importance: 1) volume of mass
18 movements entering lakes; 2) DEM datasets; 3) the origin of mass movements; 4) mesh size;
19 5) basal frictional angle; and 6) entrainment coefficient. The volume of mass movement
20 impacting lakes has the greatest impact on GLOF output, with an average coefficient of
21 variation (CV) = 47%, while the internal friction angle had the least impact (CV=0.4%). We
22 recommend that future GLOF modelling should carefully consider the output uncertainty
23 stemming from the sensitive input parameters identified here, some of which cannot be
24 constrained before a GLOF and must be considered only statistically.



25 **1 Introduction**

26 Glacial lakes can store millions of cubic meters of water: as of 2015, it is estimated that glacial
27 lakes ($\geq 0.05 \text{ km}^2$) store about $\sim 105.7 \text{ km}^3$ of water globally (Zhang et al., 2023a; Shugar et
28 al., 2020; Zheng et al., 2021b). Although glacial lakes in High Mountain Asia (HMA) contribute
29 only 4.6 km^3 to this total volume, they have experienced the greatest expansion (46%)
30 between 1990 and 2018 (Shugar et al., 2020). Furthermore, over 28% of glacial lakes in the
31 HMA are dammed by loose/destabilizing moraines (Fujita et al., 2013; Zheng et al., 2021b)
32 and the majority of glacial lakes (70%) are exposed to mass inputs, in the form of ice/snow
33 avalanches, rockfalls and landslides (Dubey et al., 2023). Although there is no substantial
34 evidence for an increasing trend in glacial lake outburst floods (GLOF) within existing data
35 (between 850 and 2022 CE) (Shrestha et al., 2023; Lützwow et al., 2023; Veh et al., 2022; Veh
36 et al., 2023), the GLOF frequency is expected to increase in the future (Zheng et al., 2021)
37 because the glaciers and permafrost in HMA are extremely sensitive to rising temperatures
38 (Gruber et al., 2017; Kääb et al., 2018). Meltwater resulting from the shrinkage of glaciers
39 leads to the formation of new glacial lakes and the expansion of existing ones (Zhang et al.,
40 2015; Wang et al., 2020). This process sometimes exposes them to mass movement from the
41 slopes above and increases the total volume of stored water (Rounce et al., 2016).
42 Additionally, the degradation of permafrost destabilizes the slopes surrounding the glacial
43 lakes, increasing the likelihood of mass movements into lakes (Huggel, 2009).

44 Recent work has documented 3151 GLOF events between 850 and 2022 C.E. globally
45 (Lützwow et al., 2023) and 682 GLOF events in HMA between 1833 and 2022 (Shrestha et al.,
46 2023). In the HMA alone, these GLOF events have resulted in 6907 human deaths, caused
47 damage to more than 2200 buildings, 71 km^2 of agricultural land, 163 MW capacity of
48 hydropower, 2000 livestock and numerous other structures, including bridges and roads
49 (Shrestha et al., 2023). However, these reported deaths and damages are significantly
50 underestimated because of patchy documentation (Carrivick and Tweed, 2016). Unfortunately,
51 the risk from GLOF is expected to rise in the future with the anticipated expansion of glacial
52 lakes (Zheng et al., 2021b; Zhang et al., 2023b) compounded by a growing population and the
53 construction of structures in areas prone to GLOFs (Taylor et al., 2023; Nie et al., 2023).

54 Most GLOF events in HMA start with mass movements entering the lake from surrounding
55 slopes, leading to the displacement of water and waves overtopping the dam (Shrestha et al.,
56 2023; Lützwow et al., 2023; Nie et al., 2018). Rock- or ice-avalanches and landslides entering
57 the lake constitute 70% of known causes of HMA historical GLOF events (Shrestha et al.,
58 2023). The overtopping waves cause moraine dam incision and dam failure, resulting in a
59 sudden discharge of lake water. To a lesser extent, GLOF events are also triggered by factors



60 such as increased hydrostatic pressure from runoff snow and ice melt, intense rainfall and
61 cloud outbursts, and dam settling caused by the melting of ice cores or internal piping. As the
62 flood propagates further downstream, it can transform into a debris flow and/ or a hyper-
63 concentrated flow/debris flood depending on the geologic and topographic characteristics of
64 the river channel (Gaphaz, 2017; Schneider et al., 2014; Westoby et al., 2015; Westoby et al.,
65 2014). These complex GLOF process chains are difficult to accurately capture in numerical
66 models, given the large number of processes and parameters, and the phase transformations
67 during the event, which limits our ability to model the impacts of the hazard cascade as a
68 whole.

69 **1.1 Numerical modelling of GLOFs**

70 Previous studies have used various modelling codes such as HEC-RAS (Sattar et al., 2021b),
71 BASEMENT (Worni et al., 2013; Worni et al., 2012; Byers et al., 2018), FLO-2D (Somos-
72 Valenzuela et al., 2015), RAMMS (Lala et al., 2018), and r.avaflow (Mergili et al., 2020b). Most
73 all these models, however, cannot model the evolution of the GLOF process chain through
74 interaction at the boundary of different processes involved (e.g. the interaction of mass
75 movements with the lake) and dynamic transformation of flow through entrainment and
76 deposition. To address this limitation, some of the studies modelled each component
77 separately and then fed the results of each modelling component into the next stage (Lala et
78 al., 2018; Schneider et al., 2014; Frey et al., 2018). For example, Lala et al (2018) have used
79 RAMMS to model mass movement from the surrounding slope into the lake, Heller–Hager and
80 BASEMENT to model wave propagation across the lake surface and BASEMENT to model
81 the subsequent downstream hydrodynamic evolution of GLOF. In contrast, the r.avaflow model
82 (Mergili et al., 2017; Mergili and Pudasaini, 2024) enables the integration of all components of
83 the GLOF process chain and their interactions and transformation without the need to combine
84 the results of different models. It enables the detailed modelling of the GLOF process chain,
85 covering everything from the initial trigger to the downstream propagation. r.avaflow is an
86 open-source, GIS-based tool for simulating mass flows over arbitrary terrain. Furthermore,
87 r.avaflow is open source and allows modification of all input parameters, making it suitable for
88 conducting GLOF parameter sensitivity analysis (Mergili et al., 2017; Mergili and Pudasaini,
89 2024).

90 r.avaflow utilizes the total variation diminishing non-oscillatory central differencing (NOC-TVD)
91 numerical scheme (Wang et al., 2004) to solve an enhanced version of the Pudasaini multi-
92 phase flow model (Pudasaini and Mergili, 2019). It also offers added features for entrainment,
93 deposition, dispersion, and phase transformation. Because of these features, r.avaflow can
94 model the full process chain of a GLOF and flow transformation due to erosion of bed material



95 and deposition of entrained material (Mergili et al., 2017; Mergili and Pudasaini, 2024).
96 However, the precision of this model output depends on the accuracy of various input
97 parameters and initial conditions, including the release height of mass, the resolution and
98 vertical accuracy of the digital elevation model (DEM), density, entrainment, and frictional
99 parameters (Mergili et al., 2017). The difficulty involved in getting accurate measurements of
100 these parameters introduces substantial uncertainty in the modelling results.

101 Because of the significant logistic challenges associated with collecting field data and the
102 financial costs involved in acquiring high-resolution remote sensing data, many of the
103 parameters in GLOF modelling are derived from open-access data, leading to considerable
104 uncertainties in the resultant discharge, inundation extent, and arrival times. Also, certain
105 factors such as the volume of mass movement entering the lake are impossible to measure
106 accurately before a GLOF event. For example, the global-scale DEM, SRTM GL1, with a
107 ground resolution of 30 m, is commonly employed in GLOF modelling without adequately
108 considering the inherent uncertainty due to horizontal and vertical inaccuracies in this DEM
109 (Rinzin et al., 2023). Similarly, the origin of avalanches and other mass movements is
110 determined using low to medium-resolution remote sensing imagery and DEM, often
111 supplemented by secondary datasets like permafrost data (Obu et al., 2019), which can
112 introduce notable uncertainties (Sattar et al., 2023; Allen et al., 2016). When estimating the
113 volume of avalanches entering lakes, DEM differencing between pre- and post-event
114 conditions can be advantageous for reconstructing historical events (Baggio et al., 2021;
115 Zheng et al., 2021a), although the accuracy is contingent upon the vertical and horizontal
116 accuracy and resolution of the data, and the temporal interval between data acquisition.
117 Likewise, when ice is considered the sole source of avalanches, ice thickness is employed to
118 calculate the avalanche volume (Allen et al., 2022), for which the accuracy of computed
119 volume relies on the resolution and availability of data in the region of interest. Under the
120 circumstances when the depth of landslides and avalanches are not known, conservative
121 thicknesses of 10, 30, and 50 m based on past events (Dubey et al., 2023) are often utilised
122 for forward modelling, further contributing to significant uncertainties in the modelling results
123 (Rounce et al., 2017; Rounce et al., 2016; Dubey and Goyal, 2020).

124 Moreover, the flow parameters in *r.avaflow* are adjusted and optimised based on the fit of the
125 model's results to well-documented past events (Mergili et al., 2017; Mergili et al., 2020a; Vilca
126 et al., 2021) and the physically plausible range suggested by Mergili et al. (2017), Mergili et
127 al. (2018b) and Mergili et al. (2018a). Efforts to fine-tune parameters to fit with historical events
128 of varying magnitude, temporality and spatiality have led to the use of wide-ranging values.
129 For example, Mergili et al. (2020b) used an internal solid friction angle of 28° to reconstruct



130 the 1941 GLOF process chain of Lake Palcacocha in the Cordillera Blanca, Peru. In contrast,
131 Vilca et al. (2021) used 45° to model the 2020 glacial lake outburst process chain of Lake
132 Salkantycocha located in Cordillera Vilcabamba of Peru. Likewise, the value of the basal
133 friction angle ranges between $6-18^\circ$ (Baggio et al., 2021; Mergili et al., 2020a) (Supplementary
134 Figure 1 (Fig. S1)). Because each GLOF event is inherently distinct, even when originating
135 from the same glacial lake (Emmer and Cochachine, 2013; Lala et al., 2018), employing
136 reconstructed values from past events for forward modelling introduces substantial
137 uncertainties (Gaphaz, 2017; Mergili et al., 2020b). Finally, r.avaflow model outputs are
138 extremely sensitive to parameters like entrainment coefficient value, basal friction angle and
139 initial release volume (Mergili et al., 2018b; Mergili et al., 2018a; Baggio et al., 2021). However,
140 to our knowledge, how changes in the values of these input parameters affect the model output
141 (for example, peak and total flow, flow depth, flow velocity and arrival time) is not known.

142 To determine the relative contribution of uncertainties in different input parameters to variability
143 in GLOF extent, we identified nine out of 38 input parameters and initial conditions relevant to
144 GLOF flow modelling that have been previously identified as the most important in the
145 literature: digital elevation model; mesh size; the volume of mass movement impacting the
146 lake; the origin of mass movement impacting the lake; grain density of mass movement
147 impacting the lake; entrainment coefficient; internal friction angle; basal friction angle; and,
148 fluid friction number (Table S1). We assessed the sensitivity of the model output to each of
149 these parameters by conducting up to 10 r.avaflow simulations per parameter and varying
150 their values within the range determined from the literature that employed r.avaflow modelling
151 (Fig. S1). We investigated the impact of variation in these parameter values on the model
152 outputs and used the following diagnostic variables: peak discharge; total discharge; flow
153 arrival time; flow height; flow velocity and reach distance. We then calculated the coefficient
154 of variation for each parameter and ranked them based on this metric.

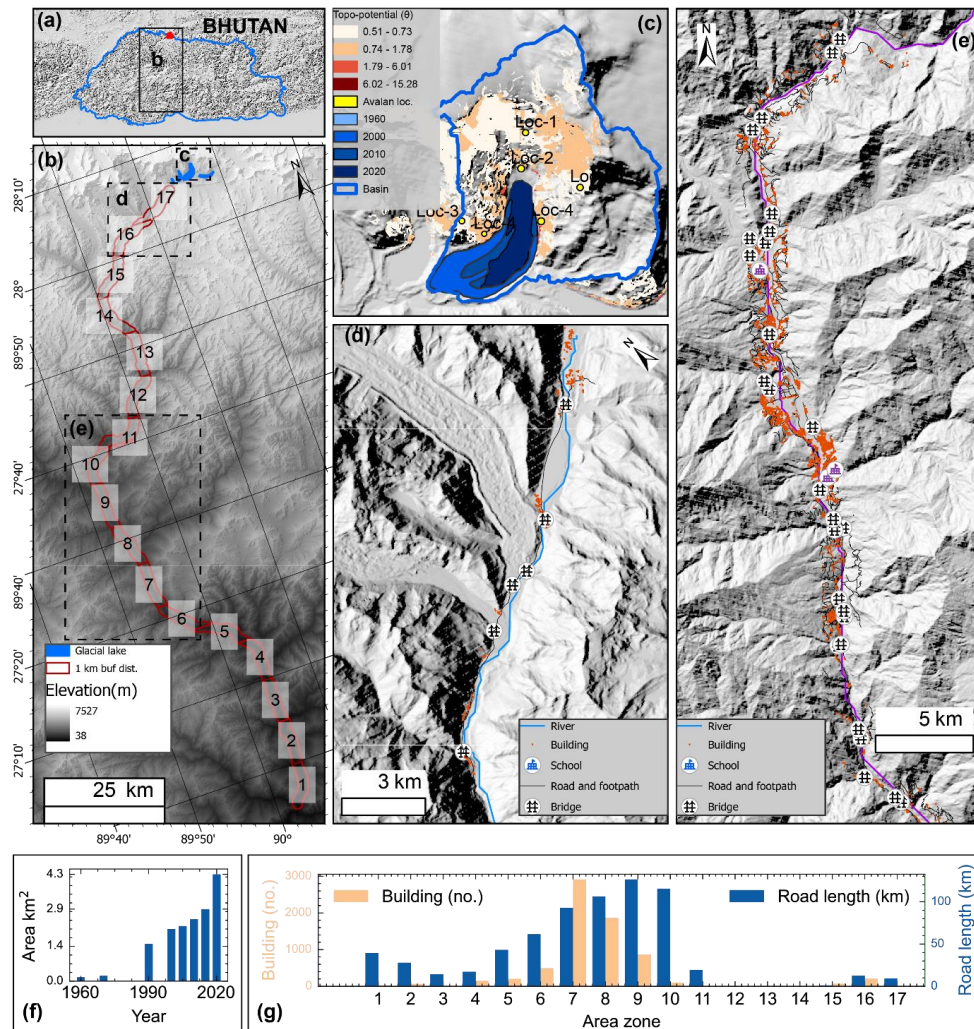
155 **2 Study site**

156 Here, our sensitivity analysis is conducted on Thorthormi Tsho located at 28.10° N, 90.27° E
157 in the Lunana region of the Bhutan Himalaya (Fig. 1). The area of Thorthormi Tsho has
158 expanded by $\sim 192\%$ since 1990, evolving into the largest proglacial lake (area = 4.35 km^2)
159 in Bhutan by 2020 (Rinzin et al., 2023) (Fig. 1B and 1E). Although the lake level was lowered
160 by 5m by artificially draining out the water between 2008 and 2012 (Nchm, 2019a),
161 Thorthormi Tsho is marked as the most dangerous glacial lake (Nchm, 2019a; Rinzin et al.,
162 2021) (Fig. 1B). In recent years, Thorthormi Tsho has produced two GLOF events (Nchm,
163 2023); the first one occurred on June 20, 2019 (Nchm, 2019b), the latest on October 30,
164 2023. Also, modelling of future predicted GLOF from Thorthormi Tsho shows it can produce



165 a flood with flow volume up to $300 \times 10^6 \text{ m}^3$ of water with a peak discharge of up to 75000
166 $\text{m}^3 \text{ s}^{-1}$, affecting more than 16000 people and various infrastructures downstream of this
167 glacial lake (Rinzin et al., 2023). This high outburst susceptibility and potential make
168 Thorthormi Tsho an ideal candidate for GLOF modelling to improve our modelling output

169 GLOF uncertainty.



170

171 **Figure 1:** Study area. The map (a) location of Thorthormi Tsho and its downstream condition
172 in Bhutan. The map (b) shows elevation and the overview of glacial lakes in Lunana and
173 settlements along the Phochu and Punatsangchu basins, downstream of Thorthormi Tsho.
174 The downstream settlement is divided into 17 zones (1-17), each 10 km long. (c) Area of
175 Thorthormi Tsho between 1960 and 2020, and the surrounding slope with topography potential



176 (TPP) for mass movement entering Thorthormi Tsho. (d and e) the downstream settlements
177 in the (d) Lunana and (d) Punakha and Wangdue Phodrang regions. The bar graphs are (f)
178 the change in the area of Thorthormi Tsho between 1960 and 2020 and (g) the buildings
179 (count) and road (km) within the 1 km on either side of the river centreline as per the latest
180 OpenStreetMap.

181 Additionally, the Phochu and Punatsangchu basins, located downstream of Thorthormi Tsho,
182 are the most populated basins in Bhutan. The latest updated OpenStreetMap,
183 (<https://www.openstreetmap.org>) although it does not have 100% coverage, shows that there
184 are over 7000 buildings, 50 bridges, 4 schools, 687 km of road and a large area of agricultural
185 land within the 1 km radius of the Phochu and Punatsangchu rivers. 202 buildings are located
186 within the immediate 10 km downstream of Thorthormi Tsho (Fig. 1c,1d,1f). Besides, located
187 downstream are the two biggest hydropower plants (Punatsangchu-1 and Punatsangchu-2)
188 in Bhutan nearing the commission and poised to become key contributors to the nation's GDP.
189 Also, the Punakha Dzong, great historical and cultural significance is located downstream of
190 Thorthormi Tsho. This high downstream exposure to GLOF hazard further highlights the
191 importance of understanding GLOF characteristics from Thorthormi Tsho for GLOF modelling
192 (Fig. 1).

193 **3 Methods**

194 **3.1 r.avaflow model framework**

195 r.avaflow is a comprehensive GIS-based open-source computational framework for modelling
196 mass movement from one or more release areas over the defined basal topography (Mergili
197 et al., 2017; Mergili and Pudasaini, 2024). It can model the entire GLOF process chain starting
198 from the release of avalanches, through the dynamic interaction of the avalanche and lake
199 water, then the overtopping and retrogressive moraine dam erosion, and finally the
200 downstream evolution of the resulting flow (Mergili et al., 2020b; Vilca et al., 2021; Sattar et
201 al., 2023). It can also robustly consider the interactions between the phases as well as erosion
202 and deposition (Mergili et al., 2017). Furthermore, it is equipped with a built-in function for
203 visualization and validation. Because of this capability, r.avaflow has been widely used to
204 model process chains such as GLOF in the high mountains all over the world, mostly to
205 reconstruct past events (Zheng et al., 2021a; Mergili et al., 2020b; Vilca et al., 2021) and to a
206 lesser extent to predict future hazards (Sattar et al., 2023; Allen et al., 2022).

207 In r.avaflow, the evolution of the flow in space and time is solved by using an enhanced version
208 of the Pudasaini multiphase flow model (Pudasaini and Mergili, 2019; Pudasaini, 2012). The
209 flow is computed through depth-averaged conservation of mass and momentum equations for



210 solid and fluid components. These equations involve six differential equations accounting for
211 solid (D_s) and fluid (D_f) flow depths, solid (M_{sx}) and fluid (M_{fx}) momentum in x direction ($M_{sx} =$
212 $D_s \cdot v_{sx}$, $M_{fx} = D_f \cdot v_{fx}$), and M_{sy} and M_{fy} in y direction ($M_{sy} = D_s \cdot v_{sy}$, $M_{fy} = D_f \cdot v_{fy}$), where v is the
213 flow velocity (Mergili et al., 2017). Mohr-Coulomb plasticity is used to compute solid stress
214 while fluid is subjected to solid volume-fraction-gradient-enhanced non-Newtonian viscous
215 stress. *r.avaflow* also considers other factors like virtual mass force, viscous drag, and
216 buoyancy. These factors collectively facilitate momentum transfer between the solid and fluid
217 phases, enabling simultaneous deformation, separation, and mixing of phases as they
218 propagate across the mountain topography (Pudasaini and Mergili, 2019; Pudasaini and
219 Krautblatter, 2014a; Mergili et al., 2020b; Pudasaini, 2012). To numerically solve these
220 differential equations and propagate flow over time and space, *r.avaflow* uses a high-resolution
221 total variation diminishing non-oscillatory central differencing (TVD-NOC) scheme, a
222 commonly used numerical scheme to handle the advection of quantities, whilst minimising
223 numerical artefacts like oscillations (Wang et al., 2004). The internal friction angle and basal
224 friction angle, which are crucial factors governing the frictional forces influencing flow rheology,
225 are scaled with a solid fraction of the flow material (Mergili et al., 2018b; Mergili et al., 2017;
226 Pudasaini and Mergili, 2019). This scaling effectively accounts for the reduced interaction
227 between solid particles and the basal surface within flows rich in fluid (Mergili et al., 2018b;
228 Mergili et al., 2017).

229 *r.avaflow* has three different models, namely, a single-phase shallow water model with Voellmy
230 friction relation, an enhanced version of the multi-phase-flow of Pudasaini and Mergili (2019)
231 and an equilibrium-of-motion model for the slow-flow process (Mergili et al., 2017). Here, we
232 chose an enhanced version of the multi-phase-flow model considering an erodible moraine
233 dam and rock-ice avalanche as the solid component and lake water as the fluid component.
234 The multi-phase mass flow model can simulate the propagation of three different elements:
235 solid (coarse material including boulders, cobbles and gravel), fine solid (including sand and
236 particles larger than clay and silt), and fluid (including water and very fine particle including
237 clay, silt and colloids), and assign each of them with distinct flow rheology (Pudasaini and
238 Mergili, 2019).

239 Furthermore, *r.avaflow* has six specific optional functions including conversion of release
240 height to depth, diffusion control, surface control, entrainment, stopping and dynamic adaption
241 of friction parameters (Mergili and Pudasaini, 2024). The latest version of *r.avaflow* has four
242 options to compute erosion and entrainment, (i) calculated by multiplying the entrainment
243 coefficient with flow momentum, (ii) simplified entrainment-deposition numerical model of
244 Pudasaini and Krautblatter (2014b), (iii) a combination of (i) and (ii), and (iv) acceleration-



245 deceleration entrainment and deposition model. Since models (ii) to (iv) are at the
 246 experimental phase, here, we used model (i), where the amount of entrainment is computed
 247 dynamically by multiplying with the user-defined entrainment coefficient (CE) with the total
 248 momentum of the flow at the given raster cell and time step (Mergili et al., 2017) (equations 1
 249 and 2).

$$q_{E,s} = C_E |M_s + M_f| \alpha_{s,Emax} \quad (1)$$

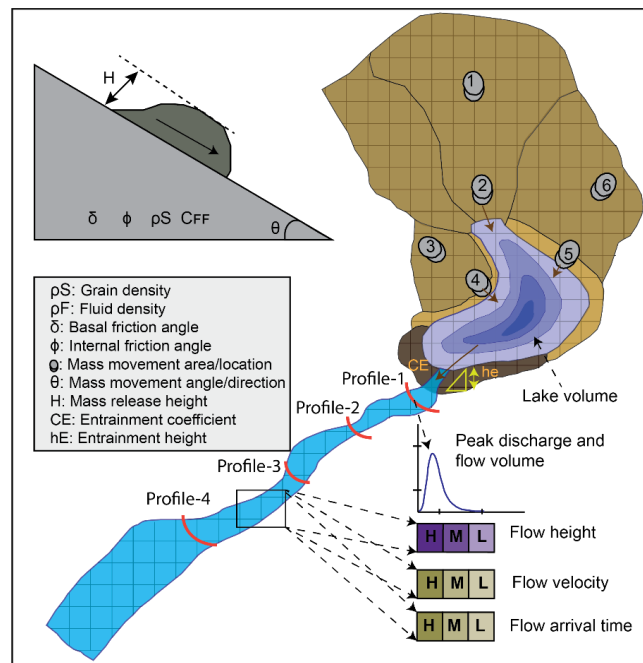
$$q_{E,f} = C_E |M_s + M_f| (1 - \alpha_{s,Emax}) \quad (2)$$

250

251 Where q_{Es} and q_{Ef} are the entrainment rates of solid and fluid respectively

252 C_E is user user-defined entrainment coefficient (kg^{-1})

253 $\alpha_{s, Emax}$ is using user-defined solid entertainable material height (m)



254

255 **Figure 2:** Schematic view of Thorthormi Tsho, surrounding terrain (study area) and input
 256 parameters employed for investigating r.avaflow model output sensitivity used in this study. 1-
 257 6 shows the location of the mass movement areas into the lake.



258 We utilized *r.avaflow direct* (Mergili and Pudasaini, 2024), a web-based tool, to initially
 259 generate the sample model script. We modified it by inputting parameters relevant to each
 260 experimental set-up and wrote a bash shell script for all simulations in each experiment to test
 261 various parameter values within our predefined range. We developed one master bash script
 262 for each experiment that allowed us to run all experiments in parallel leveraging the Rocket
 263 High Performance Computing (HPC) facilities at Newcastle University. All the GLOF
 264 simulations were done for Thorthormi Tsho and were run for 1500 seconds when the flow
 265 reaches up to ~24 km downstream of the lake depending on values of various parameters
 266 defined here. The flow propagation beyond this point and its interaction with the downstream
 267 component are beyond the scope of this study.

268 **Table 2:** Key parameters tested in this study to investigate model output sensitivity. Detailed
 269 parameters for *r.avaflow* modelling are provided in Table S1.

Parameter	Value range	No. of simulations	Constant value
Topographic data (DEM) and Mesh size	High Mountain Asia DEM (HMA-DEM) (8m), AW3D30 (30m), NASADEM (30m), SRTM GL3 (90 m)	12 (3×4)	HMA-DEM
Avalanche origin location	Left (2), Right (2), Headwall (2)	6	Loc-1
Avalanche volume	$1 - 10 \times 10^6 \text{ m}^3$	10	$5 \times 10^6 \text{ m}^3$
Grain density	$1000 - 2700 \text{ kg/m}^3$	10	2700
Entrainment coefficient	$-5.85 - -6.95 \text{ kg}^{-1}$	10	-6.35
Basal friction angle	$10 - 14^\circ$	10	10
Internal friction angle	$25 - 35^\circ$	10	28
Fluid friction number	$0.027 - 0.050$	10	0.05

270 **3.2 Model inputs parameterisation and experimental setups**

271 *r.avaflow* has a large choice of parameters and initial conditions, such as a DEM representing
 272 initial basal topography, the volume of the solid and liquid phase, entrainment and stopping
 273 parameters and density and friction parameters (Mergili and Pudasaini, 2024) (Table S1). The
 274 values specified for these parameters influence crucial aspects of modelled GLOF flow,
 275 including impacted area, travel distance, travel time, and volume of sediment deposited at the



276 various downstream locations (Mergili et al., 2017). In this study we selected a total of nine
277 parameters which are identified as important in the previous studies (e.g. Mergili et al.
278 (2020a)): 1) DEM dataset, 2) mesh size; 3) the origin of mass movement into the lake; 4)
279 volume of mass movement entering the lake; 5) grain density of mass movement entering the
280 lake; 6) entrainment coefficient; 7) basal friction angle; 8) internal friction angle; 9) fluid
281 frictional number. To investigate the impact of DEM dataset variation (1) and mesh size
282 variations (2), we modelled GLOF by employing freely available global and regional DEM
283 datasets with differing spatial resolution and vertical accuracy (Table 2). For the origin of the
284 mass movement entering lake (3), we first computed the topographic potential for slope
285 movement into the lake (Allen et al., 2019) (Fig. 1B) and selected six different sites by
286 considering the topographic potential values and direction of the lake (Fig. 2). The volume of
287 mass movement entering lake (4) was varied between $1 \times 10^6 \text{ m}^3$ and $10 \times 10^6 \text{ m}^3$. The
288 avalanche grain density (ρ_S) (5) value range was considered based on assumed combinations
289 of rock and ice avalanche parts following the approach used in the earlier studies (Allen et al.,
290 2022; Sattar et al., 2023). For parameters 6-9, we gathered various values employed in
291 previous studies (Allen et al., 2022; Mergili et al., 2020a; Mergili et al., 2020b; Vilca et al.,
292 2021) and established the conservative range. In doing so, we computed descriptive statistics
293 and established the median, upper quantile value, and lower quantile for each parameter using
294 these collated values (Fig. S1). We then varied these parameter values between the
295 calculated upper quartile and lower quartile, to give 10 equally spaced values in total. This
296 range of 10 values was utilised in our 10 experiments for the respective parameter, whilst
297 holding other parameter values constant at the median value. For example, for the internal
298 friction angle (ϕ) experiment, the ϕ was varied between the upper and lower quantiles, with 10
299 increments in total, whilst holding constant the other parameter values (Table 1). An overview
300 of employed parameters and workflow is shown in Fig. 2 and Table 1, while further details on
301 the parameter range used for each experiment are provided in the following section.

302

303

304

305

306

307



308 **Table 2:** Characteristics of DEM datasets employed in this study to investigate the impact of
 309 DEM dataset variation on GLOF modelling results.

DEM dataset	Acquisition techniques	Spatial resolution	Vertical accuracy	Coverage	Survey date
AW3D30	Optical stereo images	~30 m	6.84 m (RMSE relative to ICESat in HMA) (Liu et al., 2019)	Global	2006 to 2011
NASADEM	SAR Interferometry	~30 m	5.3 m (RMSE for USA) (Liu et al., 2019)	Global	2000
SRTM GL3	SAR Interferometry	~90 m	9.51 m (RMSE relative to ICESat in HMA) (Buckley et al., 2020)	Global	2000
HMA 8m DEM	Optical stereo images	8 m	2-m (depending on the type of sensor) (Shean, 2017a)	High Mountain Asia (HMA)	2002 to 2016

310 **3.2.1 Digital elevation (1) model and mesh size (2)**

311 Here our goal is to constrain model output uncertainty stemming from the use of freely
 312 available global and regional DEM datasets. We performed a series of GLOF simulations
 313 using four open-access DEM data of various resolutions, vertical accuracy and elevation
 314 derivation methods, namely, High Mountain Asia DEM (HMA-DEM; 8 m) (Shean, 2017b),
 315 ALOS Global Digital Surface Model (AW3D30; 30 m) (Jaxa, 2021), NASADEM (~30 m) (Nasa-
 316 Jpl, 2021), and SRTM GL3 (~90 m) ((Srtm), 2013). Further to investigate the impact of mesh
 317 size variation in each DEM dataset, we performed three simulations for each DEM data by
 318 changing mesh size to 20 m, 30 m, and 40 m. The GLOF simulations for all other parameter
 319 experiments were done using HMA-DEM at 8 m resolution (Table 2).

320 **3.2.2 Volume of lake and avalanche entering lake (4)**

321 r.avaflow has the option to define the initial release volume of different phases involved in the
 322 GLOF process chain. Here, we assume GLOF was initiated by rock-ice mixed mass
 323 movement entering into the lake followed by a tsunami wave hitting the moraine damming the
 324 lake and causing moraine dam failure. Accordingly, we defined the frontal moraine damming
 325 Thorthormi Tsho as phase-1 (rock component with $\rho = 2700 \text{ kg m}^3$), mass movement entering
 326 Thorthormi Tsho as phase-2 (rock-ice component) and Thorthormi Tsho as phase-3 (fluid part).
 327 Conducting a bathymetry survey of Thorthormi Tsho is highly challenging as the lake is filled
 328 with debris and icebergs. Therefore, we considered the volume by considering the mean value
 329 ($294 \times 10^6 \text{ m}^3$) of all the volumes estimated from a total of eight area-volume scaling equations
 330 (Table S2). This same calculated volume is used as constant fluid volume across all the GLOF
 331 simulation experiments we conducted here and was not considered for sensitivity analysis.



332 However, *r.avaflow* requires spatially varying lake bathymetry to be used as fluid release
333 height rather than the absolute value of lake volume. Fortunately, Thorthormi being a recently
334 formed lake, has ice thickness data covering the extent of the lake (Farinotti et al., 2019).
335 Therefore, we computed the bathymetry of Thorthormi Tsho by subtracting ice thickness data
336 from the surface DEM (Linsbauer et al., 2016; Linsbauer et al., 2017). Assuming that the
337 present-day lake has been formed by filling the over-deepening, this ice-thickness-derived
338 bathymetry was adjusted to match the volume we calculated from the empirical equation
339 (Table S2).

340 The volume of the avalanche entering the lake serves as a fundamental parameter for defining
341 various scenarios in the forward modelling of a GLOF (for example, Allen et al. (2022) and
342 Sattar et al. (2023)). However, for the forward modelling purpose, it is difficult to predict how
343 big or small the avalanche will be. Considering these uncertainties, to test the effect of mass
344 movement of various volumes, we conducted a series of 10 experiments considering volumes
345 ranging from 1×10^6 to 10×10^6 m³ (Table 1).

346 **3.2.3 Origin of mass movement into the lake**

347 To account for uncertainties in the exact origin of mass movement into the lake, we identified
348 a total of six mass movement areas, each characterised by different directions, distances, and
349 angles to the lake (Fig. 1 and Fig. 2). To do this, we first computed topographic potential for
350 ice/rock avalanche and landslide movement into the lake based on slope and run-out trajectory
351 criteria (Allen et al., 2019). Based on this first-order estimate, we identified the six potential
352 avalanche source areas: Loc-1 (slope at ~900 m away from the headwall), Loc-2 (headwall),
353 Loc-3 (slope at the ~900 m from right moraine dam), Loc-4 (right moraine dam), Loc-5 (slope
354 at ~900 m from left moraine dam), Loc-6 (left moraine dam) (Fig. 1 and Fig. 2). We then ran
355 one scenario for each potential avalanche input location we identified.

356 **3.2.4 Grain density of mass movement entering lake (5)**

357 Our goal here is to assess the impact of the grain density of the mass movement entering the
358 lake, which serves as a proxy for the ice-to-rock ratio. Accordingly, we consistently set the
359 grain density of phase-1 (moraine) at 2700 kg m³ across all the experiments, whilst the fluid
360 density of phase-3 was also held constant at 1000 kg m³. In the earlier studies, the grain
361 density of mass movement entering the lake has been used as a proxy of the portion of an
362 ice-rock component of mass movement into the lake, which is highly uncertain (Vilca et al.,
363 2021; Allen et al., 2022). The phase separation of rock and ice components of the mass
364 movement with different densities is not well established in *r.avaflow* (Vilca et al., 2021).
365 Therefore, in this study, following Sattar et al. (2023), a portion of snow and ice in the



366 avalanche is considered fluid by adjusting the material density of the phase-2 represented by
367 the avalanche (Table S3). In our experiment set-up, this is executed by varying the density
368 value between 2700 kg m^{-3} (representing 100% rock) to 1000 kg m^{-3} (representing 100%
369 water) (Table 1).

370 **3.2.5 Entrainment coefficient (6)**

371 Material entrainment due to bed erosion can make the flow more concentrated and thus
372 increase the volume, resulting in spatial and temporal variation of flow. In the *r.avaflow* model,
373 the user must define entrainment height in the form of a raster covering the entire model
374 domain, which can be either identified using remote sensing imagery or fieldwork (Mergili and
375 Pudasaini, 2024). However, here, we considered frontal moraine damming the lake as the only
376 entrainment height (Fig. 1). The amount of entrainment itself is dependent on the user-defined
377 entrainment coefficient (C_E). In *r.avaflow* the logarithm with base 10 of the C_E must be entered
378 (Mergili et al., 2018a; Mergili et al., 2017). Here, we modelled 10 scenarios of GLOF by varying
379 C_E between $10^{-6.95}$ to $10^{-5.85} \text{ kg}^{-1}$ (Table 1).

380 **3.2.6 Frictional parameters (7-9)**

381 The internal friction angle (ϕ), basal friction angle (δ) and fluid friction number (C_{FF})
382 mechanically control the basal shear stress, internal deformation, anisotropy of the stresses,
383 and hydraulic pressure gradient of the solid constituents (Pudasaini and Krautblatter, 2014a),
384 which are essential attributes influencing flow runout distance and time. Within the *r.avaflow*
385 model set-up, a user can either use spatially varying values for these frictional parameters
386 using a raster map or one absolute value (Mergili and Pudasaini, 2024; Mergili et al., 2017).
387 In this study, we computed 10 experiments for each of these frictional parameters. Specifically,
388 by varying the ϕ between 25° to 35° , δ between 10° and 14° and C_{FF} between 0.027 to 0.050
389 (Table 1).

390 **3.3 Sensitivity Analysis**

391 Here we use sensitivity analysis, to determine how variations in the initial values for key impact
392 the model outputs (Saltelli et al., 2004). Thus, our goal is not to determine the 'correct' value
393 for each parameter but to determine the *r.avaflow* input parameter(s) that cause the most
394 variation in the model output. To constrain this variability, we mainly focused on examining the
395 peak discharge, total discharge, and flow arrival time as the output metrics. The flow for all the
396 experiments was measured from the profile immediately beneath the moraine dam (profile-1
397 in Fig. 2). We calculated the peak and total discharge based on the flow data obtained from
398 the same profile (Fig. S2). The flow arrival time was considered as the average value across



399 the time recorded from the profiles located 3 km, 6 km and 9 km downstream of the Thorthormi
400 Tsho (profile-2, 3, 4 in Fig. 2). All input parameters were standardized within a percentile range
401 of 0 to 100 for comparative analysis of their effects on the resultant outputs. For the scalable
402 parameters, we also computed simple linear regression considering input parameters as the
403 independent variable and model output as the dependent variable. To ascertain the sensitivity
404 of the model output to variations in value across all parameters, we computed the coefficient
405 of variation (CV) for individual parameters and subsequently ranked them based on this metric.
406 The CV is a statistical measurement of the dispersion of data points around the mean,
407 regardless of the units used to measure it. CV is deemed suitable here since the r.avaflow
408 output variability is caused by input parameters that are measured in different units. To
409 calculate CV, we took the standard deviation of the output value range of a particular
410 experiment (e.g. peak discharge) and divided it by the mean of the same output range (Abdi,
411 2010).

412 **4 Results**

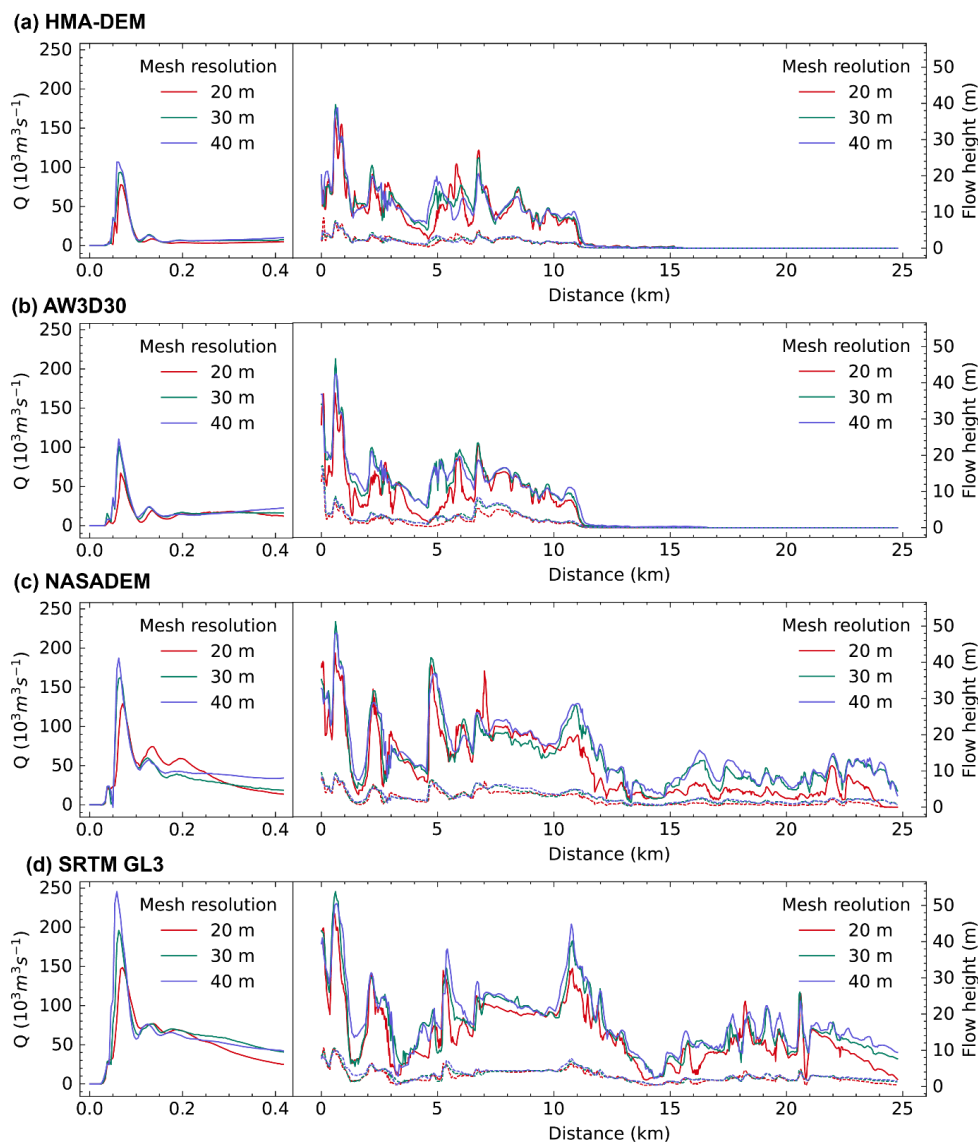
413 **4.1 Effect of DEM dataset**

414 When the GLOF is modelled employing freely available global and regional DEM datasets
415 (HMA-DEM, AW3D30, NASADEM, SRTM GL3), our results showed a variation of peak and
416 total discharge of GLOF from the Thorthormi Tsho by almost 100% and 400%, respectively
417 (Fig. 3). Specifically, HMA-DEM consistently produced the lowest GLOF magnitude, while
418 SRTM GL3 consistently produced the highest. The peak flow fluctuates between 10-115% and
419 the total discharge between 55-400% (Fig. 3). Although NASADEM and AW3D30 have a
420 similar spatial resolution, notable differences (65%) in peak discharge emerged between
421 simulations done using these datasets (Fig. 3b and 3c).

422 We observed a significant fluctuation in the mean flow height (82%) and velocity (65%) along
423 the flow path resulting from the change in DEM datasets (Fig. 3). For instance, the mean flow
424 height along the river centreline ranged from 39 m (HMA-DEM) to 54 m (SRTM GL3) (Table
425 3) and the flow reach distance increased from 15.5 km (HMA-DEM) to 24.2 km (SRTM GL3).
426 Once again, NASADEM and AW3D30 yielded significantly different maximum flow heights
427 (8.5%) and reach distances (72%) (Fig. 3b and 3c). The use of various sources of DEM
428 datasets led to variations in total flow arrival time by around 16%. Flows derived from SRTM
429 data always arrived earlier, while those using HMA-DEM consistently showed the latest arrival
430 times (Table 3). For example, at 5 km downstream, SRTM GL3 showed the earliest arrival at
431 3.46 min while HMA-DEM resulted in the latest arrival at 4.37. The portion of the solid



432 component of the flow did not exhibit significant fluctuations in response to changes in input
433 DEM datasets (Fig. 3).



434
435 **Figure 3:** Hydrographs (right panels) and maximum flow height along the river centerline (left
436 panels) generated by conducting a sequence of r.avaflow simulations, employing different
437 types of DEM datasets and varying the mesh resolution.

438 **4.2 Effect of mesh size variations**



439 When mesh size was increased from 20 m to 30 m and 40 m across all the DEM datasets,
 440 we noted a substantial increase in peak and total discharge, although changes in resulting
 441 flow characteristics like flow velocity were minimal (Fig. 3). For instance, in the case of the
 442 experiment with HMA-DEM, the peak discharges increased to 20% and 38%, respectively
 443 (Fig. 3). However, the mean flow velocity increased only by 6% when the mesh size was
 444 increased from 20 to 40 m (Table 3). Likewise, there was no significant difference in the flow
 445 reach distance emerging from changing mesh size (Fig. 3). For instance, flow with all three
 446 mesh sizes for HMA-DEM resulted in to flow reach distance of about 15 km (Fig. 3a). Mesh
 447 size variation resulted in arrival flow time variation of about 20%, with 40 m leading to earliest
 448 arrival and 20 m the latest (Table 3).

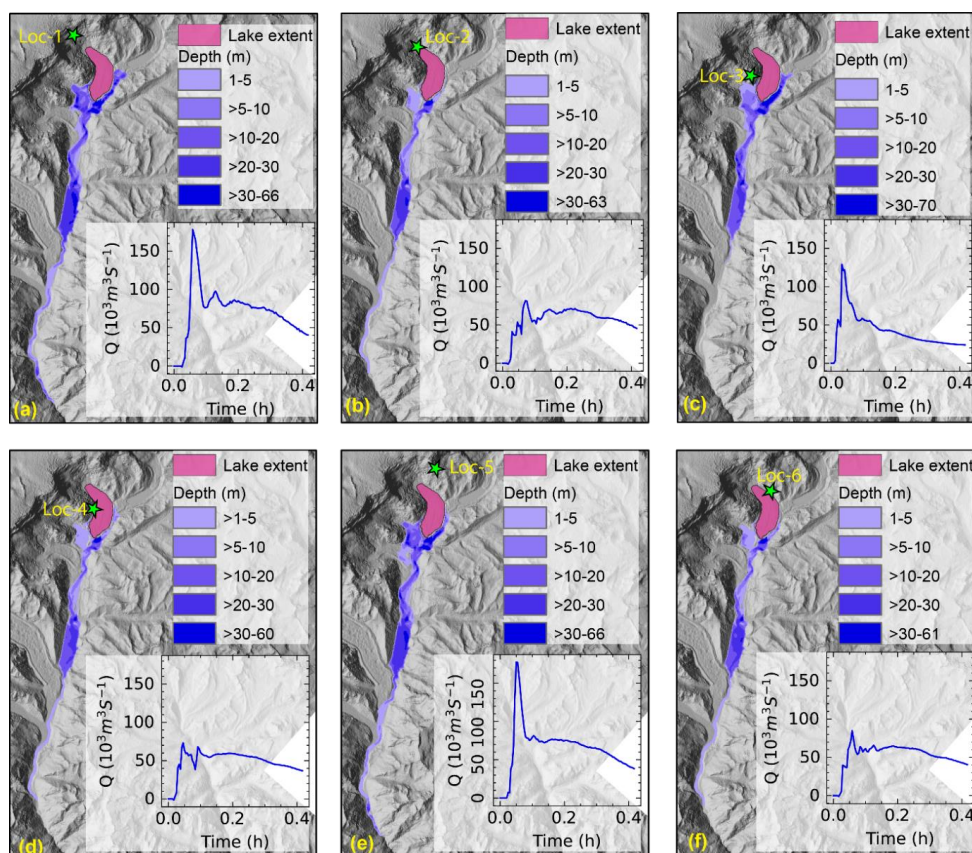
449 **Table 3.** Percentage change in flow velocity, depth and arrival time resulting from variation in
 450 values of different input parameters we employed in this study. The total percentage (%)
 451 change represents the output variation between the maximum and minimum values used in
 452 the experiment. The average percentage (%) change is calculated as the mean change across
 453 all incremental steps employed in setting up the experiment. The arrival time average of the
 454 record from three locations, Profile-2, -3, and -4) (Fig. 2). Flow velocity and depth are mean
 455 values taken from the river centreline. The detail flow pattern is provided in Fig. S3, Fig. S4
 456 and Fig. S5.

SL no.	Parameter	Velocity (% change)		Depth (% change)		Time (% change)	
		Average	Total	Average	Total	Average	Total
1	DEM dataset	16.25	65	20.5	82	4	16
2	Mesh Resolution	2	6	3	9	4	12
3	Volume of mass movement entering lake	9.2	92	92.3	923	-14.3	-143
4	Density of mass movement entering lake	0.2	2	3.1	31	6	6
5	Location of origin of mass movement entering lake	3.7	37	8.2	82	8	8
6	Entrainment coefficient	1	10	4.9	49	3	3
7	Basal friction angle	2.3	23	4.2	42	6.8	68
8	Internal friction angle	0.1	1	3.8	38	0	0
9	Fluid friction number	5.5	55	7	70	0.8	8



457 **4.3 Effect of origin of mass movement entering the lake**

458 Our study found that the GLOF process chain initiated by mass movements from various
459 locations (Loc-1 to Loc-6) results in a significant fluctuation in the GLOF output (Fig. 4). The
460 peak discharge varied by approximately 200% and the total discharge by 55% (Fig. 4).
461 Likewise, the mean flow height and velocity also fluctuated by 65% and 82%, respectively
462 (Table 3). By comparison, the flow resulting from the GLOF initiated by mass entering from
463 the Loc-1 (Fig. 4a) (900 m from the headwall) and Loc-5 (Fig. 4e) produced the highest
464 magnitude GLOF and that from the loc-4 (Fig. 4d) was the lowest. For example, the highest
465 peak ($18 \times 10^3 \text{ m}^3$) and total discharge ($11 \times 10^6 \text{ m}^3$) occurred from Loc-1, while the lowest peak
466 ($6,000 \text{ m}^3$) and total discharge ($7 \times 10^6 \text{ m}^3$) were from Loc-4 (right lateral moraine) (Fig. 4a
467 and 4d). The longest flow reach distance (25 km) was produced by loc-1 and loc-5, while the
468 shortest was from minimum from loc-3 (10 km) (Fig. 4c). Arrival times vary approximately by
469 20%, where the flow from Loc-5 arrives earlier while Loc-1 arrives at the latest (Table 3 and
470 Fig. 4). Solid volumetric portion did not exhibit significant fluctuation, with concentration
471 ranging from 4% (Loc-4) to 5% (Loc-2) (Fig. 4).



472

473

474

Figure 4: Flow rate and depth resulting from mass movement into the lake from different locations: loc-1 (a) to loc-6 (f).

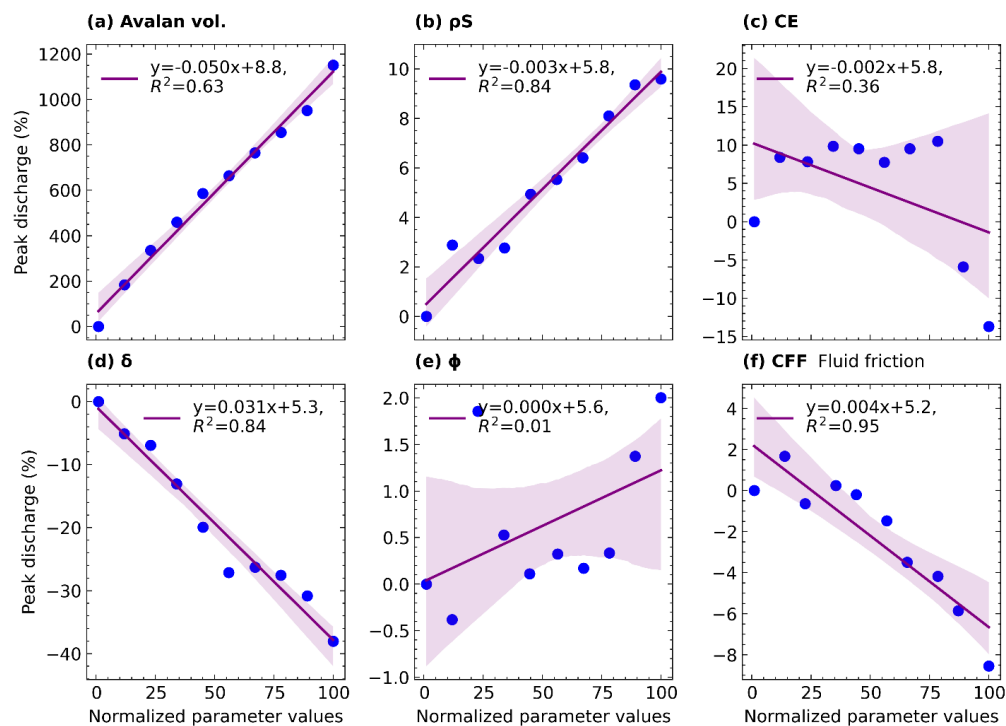
475

4.4 Effect of volume and grain density of mass movement entering the lake

476

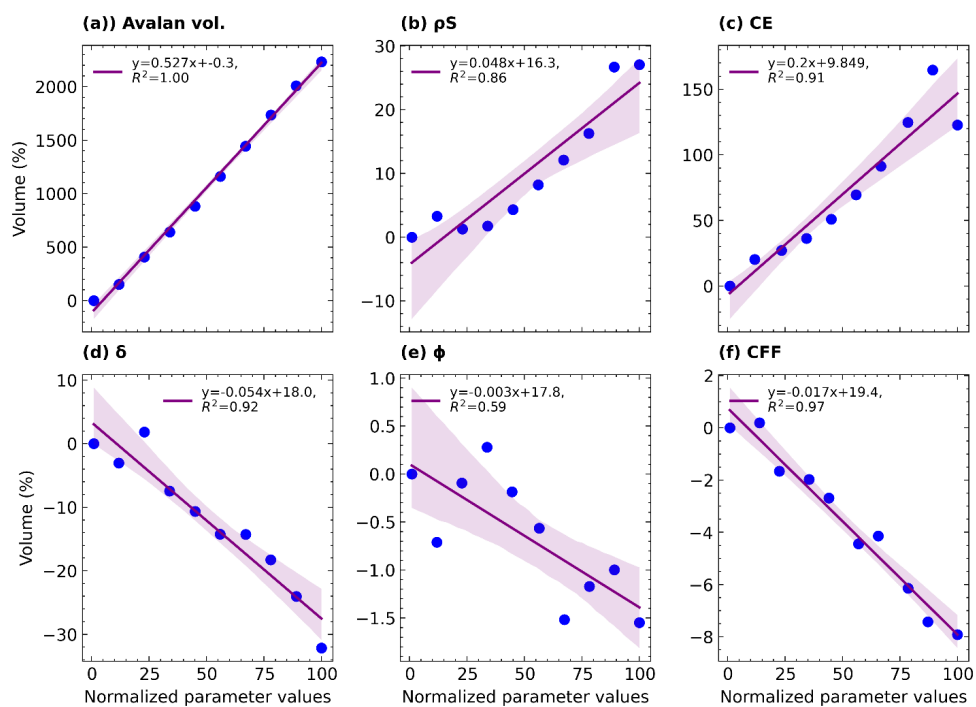
To separate the effect of variation in volume and density (ρ_S) of mass movement entering the lake, we simulated all 10 scenarios of the GLOF event using the mass movement initiated from loc-1. Here we observed that only volume variation in mass movement leads to a very large variation in the resulting peak (1160%) (Fig. 5a) and total flow (2500%) (Fig. 6a). Subsequently, this resulted in maximum variation in flow characteristics such as mean flow height (923%) and flow arrival time (50%) (Table 3, Fig. S3, Fig S5). Conversely, the ρ_S variation showed the least impact on both peak (5%) and total discharge (24%) (Fig. 5b, Fig. 6b, and Fig. 7b) and subsequent characteristics such as flow height (3%) and velocity (2%) (Table 3 and Fig. S5). Both volume and density variation did not result in significant fluctuation in the solid-volumetric concentration of the flow (Fig. S3).

485



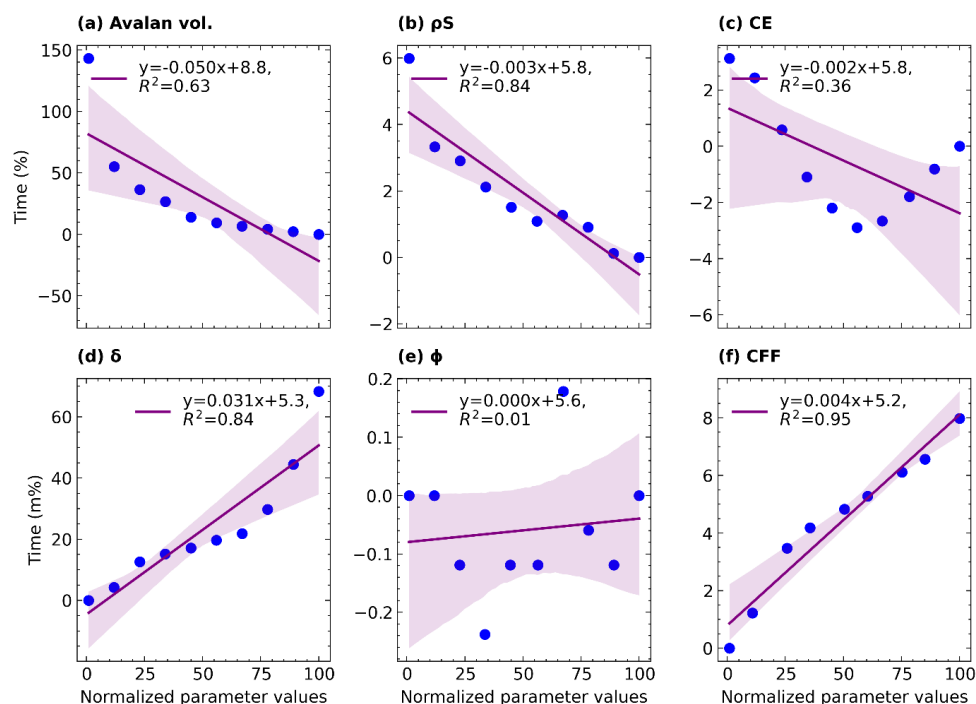
486

487 **Figure 5:** Linear regression between input parameter value variation and resulting peak
488 peak discharge. All input parameter values are normalized between 0 to 100. The linear regression
489 is computed only for the volume of mass movement into the lake (a), grain density (b),
490 entrainment coefficient (c), basal friction angle (d), internal friction angle (e) and fluid friction
491 number (f).



492

493 **Figure 6:** Linear regression between input parameter value variation and resulting total
494 discharge. All input parameter values are normalized between 0 to 100. The linear regression
495 is computed only for the volume of mass movement into the lake (a), grain density (b),
496 entrainment coefficient (c), basal friction angle (d), internal friction angle (e) and fluid friction
497 number (f).



498

499 **Figure 7:** Linear regression between input parameter value variation and flow arrival time. All
 500 input parameter values are normalized between 0 to 100. The linear regression is computed
 501 only for the volume of mass movement into the lake (a), grain density (b), entrainment
 502 coefficient (c), basal friction angle (d), internal friction angle (e) and fluid friction number (f)

503 4.5 Effect of entrainment coefficient

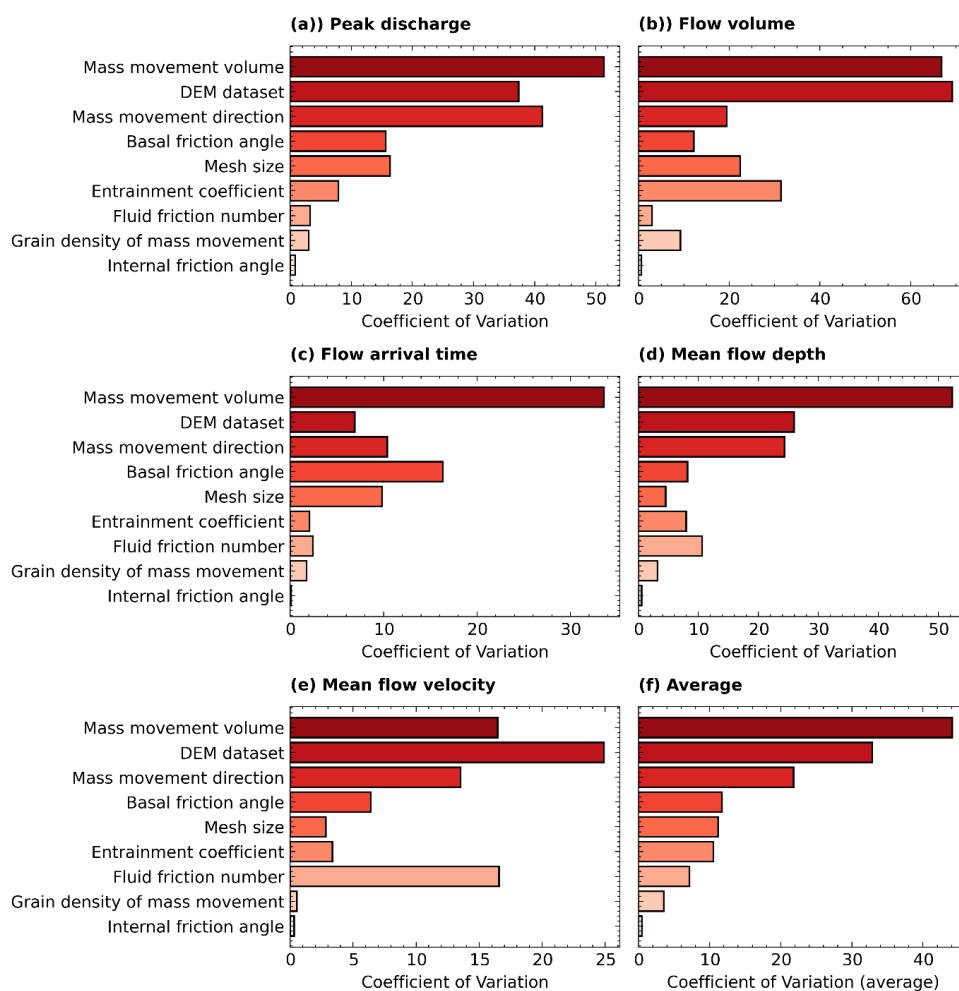
504 Variations in the entrainment coefficient substantially impact the resulting GLOF output,
 505 causing fluctuations in peak discharge and volume by 13% and 123%, respectively (Fig. 5c
 506 and 6c). These changes also affect the flow characteristics including mean depth (49%) and
 507 reach distance (20%) (Table 3) but had minimal effect on arrival time (3%) (Fig. 7c). Most
 508 notably, unlike other parameters, entrainment variation also affected the solid concentration
 509 of the flow (Fig. S3). An increase in the entrainment coefficient from $10^{-6.95}$ to $10^{-5.85}$ kg^{-1} led to
 510 a 30% increase in the mean solid volumetric concentration of the flow.

511 4.6 Effect of frictional parameters

512 Among the frictional parameters, the variation in basal friction angle (δ) resulted in a significant
 513 fluctuation in GLOF magnitude and resulting flow characteristics (Fig. 5d, 6d and 7d). While
 514 the variation of fluid friction angle had minimal impact on the resulting peak and total flow (Fig.
 515 5e, 6e), it notably altered other flow characteristics, such as flow velocity (55%) and depth



516 (70%) (Table 3). The δ angle increase from 10 to 14° resulted in a peak and total discharge
 517 decrease of 36% (Fig. 5d) and 32% (Fig. 6d), respectively. Likewise, the flow velocity
 518 decreased by 23% resulting into delay in flow arrival by 18% (Table 3). Conversely, the peak
 519 flow decreased by 2% only in response to an increase in the internal frictional angle from 25-
 520 35° (Fig. 5f). The variation in all frictional parameter values did not result in a significant change
 521 in the solid volumetric concentration of the flow (Fig. S4).



522 **Figure 8:** The coefficient of variation for (a) peak flow, (b) volume, (c) time, (d) average flow
 523 height along the river centreline, (e) flow velocity along the river centreline and (f) average
 524 across all these output parameters.
 525

526



527 **4.7 Comparison of the effect of all parameters**

528 To compare output sensitivity resulting from all parameters and initial conditions considered
529 here, we calculated the coefficient of variation (CV) for peak flow, total discharge, arrival time,
530 flow height and flow velocity. We further computed the average coefficient of variation (avg.
531 CV) across all these output variables and examined the overall impact of each input parameter
532 variation. Comparing all these output indicators, mass movement entering the lake had the
533 greatest impact (avg. CV = 47%), followed by DEM datasets (avg. CV = 35%) and the origin
534 of mass movement (avg. CV = 21%). Other input parameters like mesh size, basal friction
535 angle (δ), and entrainment coefficient also caused significant variation in resulting GLOF.
536 Notably, fluid friction number had a significant impact on flow height with its CV = 16% despite
537 having minimal impact on other flow characteristics.

538 For the six scalable parameters, we computed linear regression (Fig. 5 to Fig. 7). The linear
539 regression analysis unveiled that the four parameters, namely volume ($R^2=0.99$) of mass
540 movement into lake, ρS of mass movement into lake ($R^2=0.96$), basal friction angle (δ) ($R^2 =$
541 0.96) and C_{FF} ($R^2 = 0.83$) offer strong explanatory power regarding the variability observed in
542 resulting GLOF peak discharge (Fig. 5). Among these sets of parameters, volume ($m = 1.6$)
543 and ρS ($m = 0.085$) of mass movement entering lake indicated a positive relationship while δ
544 ($m = -0.347$) and C_E ($m = -0.091$) exhibited a negative relationship (Fig. 5). By contrast, the
545 internal friction angle ($R^2 = 0.24$) and entrainment coefficient (C_E) ($R^2 = 0.22$) exhibited a weak
546 relationship with the peak discharge. All six parameters ($R^2 > 0.9$) except for the internal friction
547 angle ($R^2 = 0.59$) indicated a high level of explanatory power regarding the variation of resulting
548 total discharge. Across all six parameters, the volume of the avalanche exhibited the highest
549 R^2 value, signifying a strong explanatory power regarding the modelled discharge volume
550 compared to the other parameters. Additionally, the substantial magnitude of the slope ($m=1.6$
551 and $m=0.53$ for peak and total discharge, respectively) associated with the volume of
552 avalanche further underscores its high magnitude relationship with the modelled GLOF flow,
553 surpassing that of the other parameters (Fig. 5a and 6a).

554 Basal friction angle δ and C_{FF} demonstrated a high level of explanatory power concerning the
555 variability in flow arrival time, as evidenced by their R^2 values of 0.98 and 0.97, respectively.
556 Avalanche volume variation also exhibited a high explanatory power with a negative
557 relationship, supported by an R^2 of 0.81 and a slope (m) of -0.019, although the linearity
558 became less pronounced within the volume range of $4 \times 10^6 \text{ m}^3$ to $10 \times 10^6 \text{ m}^3$. In contrast,
559 other parameters, including C_E , and ϕ , did not exhibit a definitive linear relationship. (Fig. 7).
560 However, CE variation showed a threshold effect on arrival time; increasing the CE from 10-



561 5.95 to $10^{-6.42}$ kg^{-1} decreased arrival time, while further increases towards $10^{-5.85}$ kg^{-1} led to a
562 linear increase in arrival time.

563 **5 Discussion**

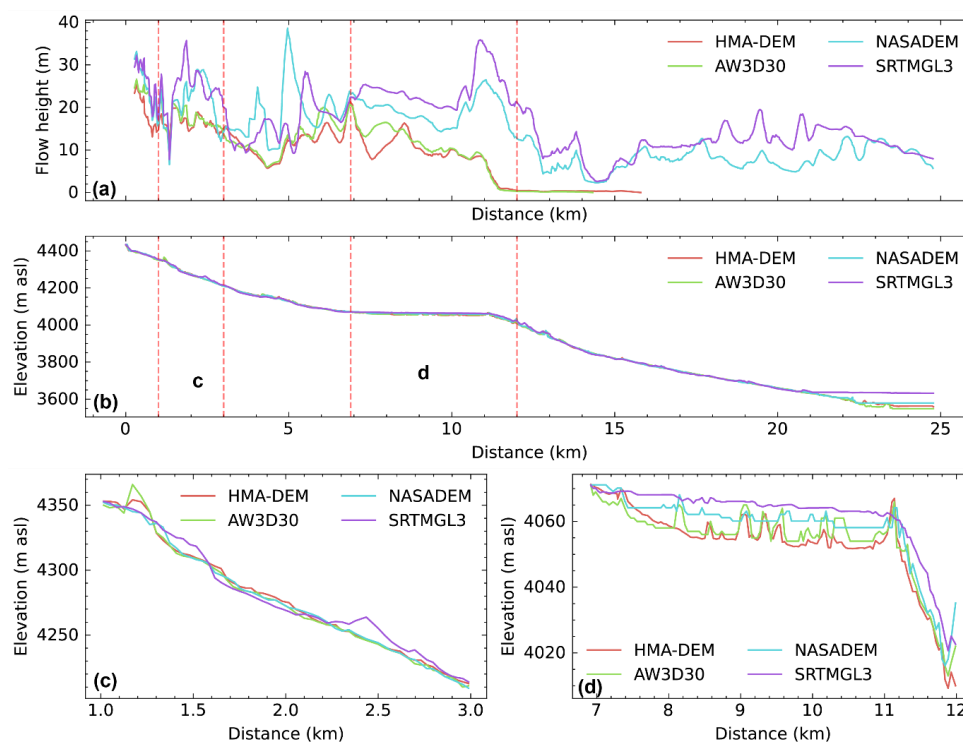
564 Our primary aim was to investigate the sensitivity of the model GLOF outputs from *r.avaflow*
565 to a range of values for key model input parameters. Previous studies have underscored the
566 sensitivity of *r.avaflow* model outputs to various input parameters, including basal friction
567 angle, entrainment coefficient and volume of avalanche entering the lake (Baggio et al., 2021;
568 Mergili et al., 2018b; Mergili et al., 2020a). This study advances our understanding of GLOF
569 modelling by conducting a comprehensive sensitivity analysis across nine parameters and
570 multiple GLOF simulations. As a result, we have for the first time, ranked these nine GLOF
571 input parameters based on their contributions to model output variabilities. Our results showed
572 that modelled GLOF output parameters are substantially sensitive to six of the nine
573 parameters we tested here (DEM dataset, mesh size, volume of mass movement into the lake,
574 origin of mass movement into the lake, entrainment coefficient, and basal friction angle)
575 suggesting that GLOF modelling results are subject to uncertainty from the multiple sources.
576 The findings offer valuable perspectives on the uncertainty of GLOF modelling results and
577 complexities inherent in modelling the GLOF process chain within the rugged mountain terrain
578 such as in the Himalaya.

579 **5.1 DEM datasets and mesh size variations**

580 DEM is one essential data for GLOF and other flood modelling (Hawker et al., 2018; Saksena
581 and Merwade, 2015; Schumann and Bates, 2018; Westoby et al., 2014). The impact of DEM
582 resolution is even more pronounced in the steep and complex topographic conditions
583 prevalent in high mountain regions like the Himalaya (Liu et al., 2019). Our study provides the
584 quantification of the effect of DEM in such environments for the first time. Our results suggest
585 that the use of global and regional DEM datasets ranging from HMA-DEM (8 m) to SRTM GL3
586 (90 m) leads to over two-fold and four-fold variations in peak and total discharge, respectively,
587 and cause successive significant fluctuations in flood height, reach distance and flow arrival
588 time. This likely results from the low-resolution DEMs not fully resolving the river channel
589 compared to higher resolution DEM, leading to reduced river channel conveyance (Fig. 9 and
590 Fig. S7) (Muthusamy et al., 2021). This was supported by a comparison of the DEM profile
591 and flow height along the river centreline (Fig. 9) and across the multiple vertical cross-
592 sections along the river channel (Fig. S6). The analysis showed that GLOF output from SRTM
593 GL3, where river channels are poorly resolved, was comparatively higher than that from the
594 HMA-DEM with the better resolved channel. Also, DEM datasets were acquired at different



595 times, meaning the topographic features they captured might also differ depending on natural
 596 geomorphological change or human-made alteration of the earth's surface over time
 597 (Schumann and Bates, 2018).



598
 599 **Figure 9:** A comparison of the elevation profiles from four DEM datasets and the
 600 corresponding flow depths along the river centreline, generated through r.avaflo modelling.
 601 panels (a) and (b) show the flow depths and elevation profiles along the river centreline.
 602 Panels (c) and (d) illustrate elevation profiles for two specific sections. DEM and flow height
 603 profiles from the vertical cross sections at various distances are also provided in the
 604 supplementary figure (Fig. S6). The DEM datasets were co-registered using Shean et al.
 605 (2016).

606 Overestimation of flood maps stemming from reductions in DEM resolution has been reported
 607 in urban flood modelling (Muthusamy et al., 2021; McClean et al., 2020). However, the impact
 608 of DEM data on GLOF modelling, especially in a complex topographic setting such as in the
 609 Himalaya has been rarely documented (Wang et al., 2011). Our results show the substantial
 610 variation in GLOF model output stemming from DEM dataset variation, even when employing
 611 DEM with comparable spatial resolutions, which underscores the criticality of high-quality DEM
 612 data in GLOF modelling (Fig. 9). DEM datasets covering rugged high mountain terrain, where



613 GLOFs typically occur are likely to have more errors due to geometric distortion and data loss
614 due to challenges involved in data acquisition for DEM production (Hugonnet et al., 2021; Liu
615 et al., 2019). Therefore, using global scale DEMs, such as SRTM and ASTER, for GLOF
616 modelling due to the absence of high-resolution alternatives (Wang et al., 2011) may only be
617 suitable for first-order assessment of GLOFs at large scales (Zhang et al., 2023b). This is
618 important as uncertainty stemming from DEM datasets is often overlooked and/or not well
619 addressed in the previous basin-specific GLOF modelling work (Rinzin et al., 2023; Sattar et
620 al., 2023; Sattar et al., 2021b).

621 **5.2 Mass movement origin variation**

622 Our study indicated that different locations of avalanche initiation produced GLOFs with
623 approximately two-fold variations in their peak discharge, volume, and reach distance (Fig. 4).
624 These variations can be explained based on the lake geometry and the direction/ angle at
625 which the mass movement enters the lake. r.avaflow model provides detailed output
626 parameters such as kinetic energy associated with the flow, and flow height map for each time
627 step, which allowed us to better understand the cause of this variation. For example, the
628 avalanche mass originating from loc-1, which is located at the slope above the headwall,
629 directly impacts the head end of the lake with the highest kinetic energy (50714 GJ) among all
630 other source avalanches. This head-end impact, coupled with its high energy, facilitates the
631 direct forward propagation of waves toward the frontal outlet, causing the lake water to overtop
632 the frontal moraine and resulting in a higher peak and total discharge (Fig. S7). Thorthormi
633 Tsho is roughly crescentic in shape and curves toward the west, with its maximum curvature
634 facing the mass movement origin of loc-6. This shape also allows the impact wave generated
635 from mass movement from loc-6 to move almost unimpeded along the flow line, resulting in
636 greater GLOF discharge. In contrast, the direct wave of impact generated by the mass
637 movement from loc-3, located on the slope above the right moraine dam, is deflected towards
638 the left lateral moraine, and only a secondary wave proceeds towards the lake outlet, resulting
639 in a comparatively lower peak and total discharge (Fig. S7). This finding implies that the
640 geometry of the glacial lake and the surrounding source slope plays a vital role in GLOF output.
641 Thus, we underscore the importance of considering catchment shape in GLOF modelling,
642 although we cannot assume that two identical basins will have the same flood properties due
643 to the influence of other factors, such as the involved volume of solid and fluid parts.

644 Earlier studies (Mergili et al., 2017; Mergili et al., 2020b) have explained the interaction
645 between landslides and reservoirs (lakes) and their influence on the resulting hydrograph.
646 However, these studies did not consider the variables such as directions and angles from
647 which the mass impacts the lake. To fill this gap, here we enhanced our understanding of the



648 interplay between the resulting GLOF magnitude and avalanche mass attributes including the
649 direction and angle from which the avalanche mass enters the lake, the amount of kinetic
650 energy the avalanche mass possesses and the geometry of the lake. Our results emphasize
651 the significant impact on the resulting GLOF events caused by the uncertainty in pinpointing
652 the specific location of origin of mass movement into the lake. Thawing of permafrost and
653 destabilization of the slope surrounding the lake due to climate warming (Gruber et al., 2017;
654 Kääb et al., 2018) combined with the expansion of the glacial lake towards the mountain flank
655 (Rounce et al., 2016) are likely to increase the frequency of mass movement into the lake,
656 further exacerbating this uncertainty. Therefore, our finding here will be useful to further
657 improve the development of scenario-based approaches to GLOF modelling (Gaphaz, 2017;
658 Sattar et al., 2021a) including, high, medium, small and worst-case scenarios (Allen et al.,
659 2022; Gaphaz, 2017).

660 **5.3 Mass movement volume, grain density, and entrainment coefficient**

661 Our investigation revealed that variation in GLOF magnitude is most sensitive to the volume
662 of avalanches entering the lakes. It also exhibits a significant level of sensitivity to the
663 entrainment coefficient whilst the grain density (ρ_S) exhibits negligible impact. For example,
664 the variation of avalanche volume between $1 \times 10^6 \text{ m}^3$ and $10 \times 10^6 \text{ m}^3$ leads to peak and total
665 discharge fluctuation of 1160% and 2500%, respectively, and subsequent variation in
666 maximum flow height and arrival time (Fig. 5 to Fig. 7). The dominant impact of avalanche
667 volume and entrainment coefficients on GLOF magnitude could be due to their direct influence
668 on the overall magnitude and intensity of flood events. The total discharge during the GLOF
669 cascade event is a function of the volume of the avalanche entering the lake. This is further
670 corroborated by the near-perfect linear relationship between peak discharge ($R^2 = 0.99$) and
671 total discharge ($R^2 = 1$) with the volume of avalanches entering the lake observed here.
672 Likewise, the volume of solid content in the flow is solely contributed by the entrainment of
673 frontal moraine material, primarily determined by the entrainment coefficient (C_E). Additionally,
674 this correlation could be attributed to the amount of energy and associated momentum of the
675 flow, which changes significantly with corresponding variations in avalanche volume. Also, it
676 could be due to the longer timing and duration of the flow as evident in Fig. S4. Most GLOF
677 events in high mountains across the HMA and other alpine regions are caused by moraine
678 dam breaches triggered by mass movement entering the lake from the surrounding mountain
679 flank (Shrestha et al., 2023; Lützow et al., 2023; Emmer and Vilímek, 2014). As a result, mass
680 movement volume is considered a primary basis for scenario development (Allen et al., 2022).
681 Thus, we believe this finding provides useful insights towards improving the developing of



682 different scenarios of GLOFs with higher confidence, or is a basis for ensemble testing, with
683 the caveat that the range of outputs may be too wide to be of practical use.

684 **5.4 Frictional parameters variations**

685 Among the frictional parameters, our result showed that GLOF magnitude is most sensitive to
686 the δ . For example, the variation of total discharge (47.5%) resulting from fluctuation of δ within
687 the conservative range was 30 times greater than that of internal friction angle (ϕ) and over
688 four times greater than that of fluid friction angle (C_{FF}). δ plays a dominant role in flow dynamics
689 and the interaction between the flowing material and the channel bed. This direct contact
690 means that even minor changes in δ can have substantial effects on the resistance
691 encountered by the flowing material, thereby influencing the mobility of the flow (Pudasaini
692 and Krautblatter, 2014b; Mergili et al., 2018a; Mergili et al., 2018b). ϕ on the other hand
693 primarily affects particle interactions within the flowing material, whilst C_{FF} is a coefficient which
694 quantifies the overall flow resistance within the flow path mainly depending on surface
695 roughness. Our findings indicate that prioritizing the consideration of δ over the other two
696 frictional parameters is advisable. This can be done by determining spatially variable values
697 through field data or conducting a statistically substantial sensitivity analysis. Nonetheless,
698 despite the relatively low overall impact on GLOF magnitude, the C_{FF} notably increased the
699 flow's mobility, especially beyond 12 km downstream, when the flow became fluid-dominant
700 (Fig. S4). This because C_{FF} is controls the mobility of the fluid part (Mergili and Pudasaini,
701 2024; Mergili et al., 2017). This suggests that C_{FF} could exert a substantial influence,
702 particularly in modelling scenarios encompassing longer flow distances.

703 **5.5 Key points from the comparison of all parameters and the way forward**

704 Identifying the most accurate parameter values or optimal datasets can be achieved through
705 validation with well-constrained historical events (Zheng et al., 2021a; Schneider et al., 2014;
706 Mergili et al., 2020b; Shugar et al., 2021), but there are limitations in the transferability of these
707 findings due to the unique characteristics and initial conditions of each GLOF, such as varying
708 volumes of solid and liquid. These specific conditions mean that the results of one modelled
709 GLOF event might not accurately predict the behaviour of GLOFs in different regions or under
710 different circumstances (Mergili et al., 2018a; Mergili et al., 2020b). Therefore, while these
711 back-analysed parameter values can provide valuable insights, they need to be applied with
712 caution and adapted to the specific context of each new GLOF scenario. This is emphasized
713 by our finding that the characteristics of the modelled GLOF are substantially impacted by
714 various parameters. As a result of these multiple sources of uncertainty in modelled GLOF, it
715 could pose challenges in effectively communicating risks with communities and other



716 stakeholders (Thompson et al., 2020). We highlight that more sensitive parameters should be
717 treated carefully in future GLOF modelling works by robustly considering associated
718 uncertainties.

719 Due to the high sensitivity of the model output on DEM resolution, we emphasize the critical
720 importance of high-resolution and good-quality DEM (Uemaa et al., 2020; Schumann and
721 Bates, 2018), especially when modelling is aimed at producing hazard maps with higher
722 granularity at the specific basin scale. Specifically, DEMs should be the high spatial resolution,
723 high vertical accuracy and recently produced, especially in areas of high relief and rapid
724 landscape change such as in Himalaya (Schumann and Bates, 2018). Previous studies have
725 indicated that flood modelling accuracy can be improved by correcting the effect of DEM
726 resolution and accuracy (Saksena and Merwade, 2015) or by merging with other high-
727 resolution and accurate DEMs (Muthusamy et al., 2021). These methods appear viable in the
728 context of highly sparse coverage of high-resolution DEMs and the unaffordability of high-
729 resolution commercial DEMs, but the modelling results should still be interpreted with caution.
730 On the other hand, whilst it poses computational challenges, especially with high-resolution
731 DEMs, we believe that selecting a mesh size equivalent to the spatial resolution of the DEM
732 could effectively mitigate uncertainty associated with mesh size variation. Models such as D-
733 Claw which features patch-based adaptive mesh refinement capability can be potentially used
734 as alternative models, however, its use in GLOF modelling is limited so far (Iverson and
735 George, 2014; George et al., 2017).

736 Avalanche volume and δ exhibit a strong linear relationship with all output parameters. Whilst
737 the linear relationship does not negate the influence these parameters have on flow
738 characteristics, it suggests that model output errors resulting from uncertainties in these
739 parameters might be predictably managed. This is essential since predicting the volume of
740 mass movement involved in the forward modelling is highly challenging and determining an
741 accurate value is impossible – the current challenge is rather to establish a likely envelope of
742 volumes. However, such prediction should be bespoke to the particular events based on the
743 initial parameters like estimated ice thickness, slope, and presence of permafrost.
744 Furthermore, such predictions must also consider other factors, such as equifinality arising
745 from the interaction of multiple parameters (Mergili et al., 2018a; Mergili et al., 2018b; Mergili
746 et al., 2020b).

747 The C_E exhibits a linear relationship only with volume. This relationship with the volume is
748 understandable, as the entrainment coefficient is a primary determinant of how much solid
749 fraction of the flow is added due to erosions. However, the arrival time exhibits distinct
750 thresholds at the entrainment coefficient $10^{-6.46} \text{ kg}^{-1}$. The decrease in flow arrival time



751 observed until a CE value of $10^{-6.46} \text{ kg}^{-1}$ may be attributed to the flow being primarily dominated
752 by the fluid component, with the contribution from erosion being negligible. However, the
753 subsequent increase in flow arrival time as the CE value further increased from $10^{-6.46} \text{ kg}^{-1}$ to
754 $10^{-5.85} \text{ kg}^{-1}$ could be attributed to the effect of increasing concentration resulting from a higher
755 rate of erosion. This suggests that once this threshold is surpassed, the resulting peak flow
756 and arrival time demonstrate a heightened sensitivity to variations in entrainment.
757 Consequently, this sensitivity may translate to the flow characteristics such as flow height and
758 arrival and arrival time which are essential for hazard and risk assessments. It is important to
759 note that this threshold value may vary across different GLOF events due to the diverse
760 combinations of other parameters.

761 The linearity demonstrated by the initial volume of avalanches entering the lake and δ warrants
762 further investigation into flow characteristics resulting from variations in these parameters.
763 Further investigation with adequate sample sizes and a reliable statistical approach would
764 enable the establishment of accurate relationships or predictor values. The threshold effect
765 observed in the C_E value also warrants further investigation using statistically conclusive
766 samples to determine whether the threshold value is universal across different events or
767 specific to individual occurrences. For factors such as internal friction angle, fluid friction
768 number, and ρS , the conservative values may suffice or receive less emphasis, particularly
769 considering the numerous parameters involved in GLOF modelling.

770 The *r.avaflow* model provides comprehensive and open-source codes for simulating
771 cascading mass flow in complex topographies (Mergili and Pudasaini, 2024). Its
772 comprehensiveness stems from the wide range of parameters it considers, making it a
773 versatile tool for various mass flow process chain simulations (Mergili et al., 2017). Past
774 studies have demonstrated the model's ability to accurately back-calculate historical events
775 with detail (Shugar et al., 2021). However, challenges persist in its application to forward
776 modelling (Allen et al., 2022; Sattar et al., 2023), particularly in the context of GLOF hazard
777 and risk assessment (Mergili et al., 2020b). In our study, we conducted a robust sensitivity
778 analysis considering nine parameters relevant to GLOF towards addressing these challenges.
779 Since we identified the key parameters that significantly influence the modelled GLOF output,
780 our result can be used as a basis for further improvement and optimization of *r.avaflow*
781 modelling codes.

782 The GLOF simulations were conducted using the *r.avaflow* model due to its capability to model
783 the entire GLOF process chain (Mergili and Pudasaini, 2024; Mergili et al., 2017). While we
784 present the uncertainty involved in the full process chain GLOF from mass movement entering
785 the lake to downstream propagation, we specifically explored the uncertainty of the GLOF



786 input parameters relevant to r.avaflow modelling. Input parameters such as DEM datasets,
787 and the volume and density of mass movement involved in a GLOF event, might be similar
788 across different models. However, we caution that the parameters tested here do not
789 necessarily apply to all models used for GLOF modelling.

790 The flow arrival time was measured from the profile located 3 km, 6 and 9 km downstream of
791 the lake since some of our modelled GLOF terminates before proceeding further downstream.
792 This is a reasonable point as human settlement downstream of the lake is mostly concentrated
793 around this area. The variation of flow arrival time might be underestimated if the location is
794 farther downstream from the lake.

795 Here we focused on nine essential parameters in r.avaflow, which are relevant to GLOF
796 modelling. However, including inbuilt modules, initial conditions, and all flow parameters,
797 r.avaflow has more than 30 parameters (Mergili and Pudasaini, 2024) (Table S1). Thus, our
798 sensitivity analysis might have potentially overlooked the complexity of r.avaflow stemming
799 from the effect of all these parameters.

800 One-at-a-time sensitivity analysis we used here, inherently lacks consideration for parameter
801 interactions and may have potentially overlooked important relationships (Saltelli et al., 2004).
802 Moreover, due to the immense computational cost of r.avaflow, we used only 10 simulations.
803 While this number of simulations for each parameter produced substantially conclusive
804 results, we do not discount the robustness of global sensitivity analysis employing an adequate
805 sampling size. Future studies should focus on testing further r.avaflow parameters and in-
806 depth model analysis by employing a statistically sufficient sampling size.

807 **6 Conclusions**

808 GLOFs present substantial dangers to communities residing in valleys downstream of glacial
809 lakes. GLOFs involve complex cascading processes and typically occur across rugged
810 mountain terrains. Due to these complexities, modelling GLOFs necessitates extensive input
811 data, parameters, and complex modelling codes for accurate hazard and risk assessments,
812 which is inherently challenging. However, previous studies have mostly relied on open-access
813 data and are grounded in a historical event introducing significant uncertainties to the
814 modelling results. In this study, we have, for the first time, conducted sensitivity analysis
815 considering multiple GLOF parameters and ranked these inputs based on how their
816 uncertainties in input values apportion to the variation in modelling output, by employing
817 cutting-edge modelling code, r.avaflow. Our results suggested GLOF modelling outputs such
818 as peak and total discharge are substantially sensitive to variation in input values of six out of



819 nine parameters we tested here. Specifically, the modelling outputs are the most sensitive to
820 the volume of avalanches entering lakes followed by the variation in DEM datasets and the
821 location of origin of mass movement entering the lake. Other parameters like mesh size, basal
822 frictional angle, and entrainment coefficient also showed significant sensitivity. Although
823 limited to GLOF modelling with the r.avaflow model, our study emphasizes that GLOF
824 modelling results are influenced by uncertainties stemming from various sources,
825 underscoring the need for careful interpretation of the modelling results. By ranking the model
826 parameters according to their impact on model output, our study prioritizes model input
827 parameters for future modelling efforts, given the challenge of adequately constraining multiple
828 parameters. Additionally, this study lays the groundwork for a thorough investigation into the
829 most sensitive parameters, to improve our understanding of GLOF modelling.

830 **Acknowledgement**

831 This work was supported by the Natural Environment Research Council (NERC)- funded
832 IAPETUS Doctoral Training Partnership [IAP2-21-267]. We thank Dr. Sonam Wangchuk for
833 helpin us in setting experiment in the HPC.

834 **Code and data availability**

835 The r.avaflow modelling code we used here for simulating all scenarios of GLOF can be
836 accessed at: [r.avaflow | The mass flow simulation tool \(landslidemodels.org\)](#). The SRTM GL3,
837 NASADEM and AW3D30 DEMS used here can be downloaded from the OpenTopogragphy
838 at: [OpenTopography - Find Topography Data](#). The HMA-DEM can be downloaded from the
839 National Ice and Snow Data Center at: [High Mountain Asia 8-meter DEM Mosaics Derived
840 from Optical Imagery, Version 1 | National Snow and Ice Data Center \(nsidc.org\)](#).

841 **Supplement**

842 The supplement related to this article is available online at:

843 **Author contributions**

844 SR, SA. and RC conceptualized the study. SR undertook the computational studies and data
845 analysis. AS provided guidance in modelling. MM revised and provide expert opinion on the
846 study. SA, RC and AS supervised the work. All authors wrote and edited the manuscript.

847 **Competing interests**

848 The contact author has declared that none of the authors has any competing interests.



850 References

- 851 (SRTM), N. S. R. T. M.: Shuttle Radar Topography Mission (SRTM) Global [dataset],
852 <https://doi.org/10.5069/G9445JDF>, 2013.
- 853 Abdi, H.: Coefficient of variation, *Encyclopedia of research design*, 1, 2010.
- 854 Allen, S. K., Zhang, G., Wang, W., Yao, T., and Bolch, T.: Potentially dangerous glacial lakes across the
855 Tibetan Plateau revealed using a large-scale automated assessment approach, *Science Bulletin*, 64,
856 435-445, 10.1016/j.scib.2019.03.011, 2019.
- 857 Allen, S. K., Linsbauer, A., Randhawa, S. S., Huggel, C., Rana, P., and Kumari, A.: Glacial lake outburst
858 flood risk in Himachal Pradesh, India: an integrative and anticipatory approach considering current
859 and future threats, *Natural Hazards*, 84, 1741-1763, 10.1007/s11069-016-2511-x, 2016.
- 860 Allen, S. K., Sattar, A., King, O., Zhang, G., Bhattacharya, A., Yao, T., and Bolch, T.: Glacial lake outburst
861 flood hazard under current and future conditions: worst-case scenarios in a transboundary
862 Himalayan basin, *Natural Hazards and Earth System Sciences*, 22, 3765-3785, 10.5194/nhess-22-
863 3765-2022, 2022.
- 864 Baggio, T., Mergili, M., and D'Agostino, V.: Advances in the simulation of debris flow erosion: The case
865 study of the Rio Gere (Italy) event of the 4th August 2017, *Geomorphology*, 381,
866 10.1016/j.geomorph.2021.107664, 2021.
- 867 Buckley, S., Agram, P., Belz, J., Crippen, R., Gurrola, E., Hensley, S., Kobrick, M., Lavalle, M., Martin, J.,
868 and Neumann, M.: NASADEM, National Aeronautics and Space Administration, Jet Propulsion
869 Laboratory, California Institute of Technology: Pasadena, CA, USA, 2020.
- 870 Byers, A. C., Rounce, D. R., Shugar, D. H., Lala, J. M., Byers, E. A., and Regmi, D.: A rockfall-induced
871 glacial lake outburst flood, Upper Barun Valley, Nepal, *Landslides*, 16, 533-549, 10.1007/s10346-018-
872 1079-9, 2018.
- 873 Carrivick, J. L. and Tweed, F. S.: A global assessment of the societal impacts of glacier outburst floods,
874 *Global and Planetary Change*, 144, 1-16, 10.1016/j.gloplacha.2016.07.001, 2016.
- 875 Dubey, S. and Goyal, M. K.: Glacial Lake Outburst Flood Hazard, Downstream Impact, and Risk Over
876 the Indian Himalayas, *Water Resources Research*, 56, 10.1029/2019wr026533, 2020.
- 877 Dubey, S., Sattar, A., Goyal, M. K., Allen, S., Frey, H., Haritashya, U. K., and Huggel, C.: Mass
878 Movement Hazard and Exposure in the Himalaya, *Earth's Future*, 11, 10.1029/2022ef003253, 2023.
- 879 Emmer, A. and Cochachin, L.: The causes and mechanisms of moraine-dammed lake failures in the
880 Cordillera blanca, North American Cordillera, and Himalayas, *AUC Geographica*, 48, 10, 2013.
- 881 Emmer, A. and Vilímek, V.: New method for assessing the susceptibility of glacial lakes to outburst
882 floods in the Cordillera Blanca, Peru, *Hydrology and Earth System Sciences*, 18, 3461-3479,
883 10.5194/hess-18-3461-2014, 2014.
- 884 Farinotti, D., Huss, M., Fürst, J. J., Landmann, J., Machguth, H., Maussion, F., and Pandit, A.: A
885 consensus estimate for the ice thickness distribution of all glaciers on Earth, *Nature Geoscience*, 12,
886 168-173, 10.1038/s41561-019-0300-3, 2019.
- 887 Frey, H., Huggel, C., Chisolm, R. E., Baer, P., McArdell, B., Cochachin, A., and Portocarrero, C.: Multi-
888 Source Glacial Lake Outburst Flood Hazard Assessment and Mapping for Huaraz, Cordillera Blanca,
889 Peru, *Frontiers in Earth Science*, 6, 10.3389/feart.2018.00210, 2018.
- 890 Fujita, K., Sakai, A., Takenaka, S., Nuimura, T., Surazakov, A. B., Sawagaki, T., and Yamanokuchi, T.:
891 Potential flood volume of Himalayan glacial lakes, *Natural Hazards and Earth System Sciences*, 13,
892 1827-1839, 10.5194/nhess-13-1827-2013, 2013.
- 893 GAPHAZ: Assessment of Glacier and Permafrost Hazards in Mountain Regions. Technical Guidance
894 Document, Standing Group on Glacier and Permafrost Hazards in Mountains (GAPHAZ) of the
895 International Association of Cryospheric Sciences (IACS) and the International Permafrost Association
896 (IPA). 72, 2017.
- 897 George, D. L., Iverson, R. M., and Cannon, C. M.: New methodology for computing tsunami
898 generation by subaerial landslides: Application to the 2015 Tyndall Glacier landslide, Alaska,
899 *Geophysical Research Letters*, 44, 7276-7284, 10.1002/2017gl074341, 2017.



- 900 Gruber, S., Fleiner, R., Guegan, E., Panday, P., Schmid, M.-O., Stumm, D., Wester, P., Zhang, Y., and
901 Zhao, L.: Review article: Inferring permafrost and permafrost thaw in the mountains of the Hindu
902 Kush Himalaya region, *The Cryosphere*, 11, 81-99, 10.5194/tc-11-81-2017, 2017.
- 903 Hawker, L., Bates, P., Neal, J., and Rougier, J.: Perspectives on Digital Elevation Model (DEM)
904 Simulation for Flood Modeling in the Absence of a High-Accuracy Open Access Global DEM, *Frontiers*
905 *in Earth Science*, 6, 10.3389/feart.2018.00233, 2018.
- 906 Huggel, C.: Recent extreme slope failures in glacial environments: effects of thermal perturbation,
907 *Quaternary Science Reviews*, 28, 1119-1130, 10.1016/j.quascirev.2008.06.007, 2009.
- 908 Hugonnet, R., McNabb, R., Berthier, E., Menounos, B., Nuth, C., Girod, L., Farinotti, D., Huss, M.,
909 Dussaillant, I., Brun, F., and Kaab, A.: Accelerated global glacier mass loss in the early twenty-first
910 century, *Nature*, 592, 726-731, 10.1038/s41586-021-03436-z, 2021.
- 911 Iverson, R. M. and George, D. L.: A depth-averaged debris-flow model that includes the effects of
912 evolving dilatancy. I. Physical basis, *Proceedings of the Royal Society A: Mathematical, Physical and*
913 *Engineering Sciences*, 470, 10.1098/rspa.2013.0819, 2014.
- 914 JAXA, J. A. E. A.: ALOS World 3D 30 meter DEM (V3.2), *OpenTopography* [dataset], 2021.
- 915 Käab, A., Leinss, S., Gilbert, A., Bühler, Y., Gascoin, S., Evans, S. G., Bartelt, P., Berthier, E., Brun, F.,
916 Chao, W.-A., Farinotti, D., Gimbert, F., Guo, W., Huggel, C., Kargel, J. S., Leonard, G. J., Tian, L.,
917 Treichler, D., and Yao, T.: Massive collapse of two glaciers in western Tibet in 2016 after surge-like
918 instability, *Nature Geoscience*, 11, 114-120, 10.1038/s41561-017-0039-7, 2018.
- 919 Lala, J. M., Rounce, D. R., and McKinney, D. C.: Modeling the glacial lake outburst flood process chain
920 in the Nepal Himalaya: reassessing Imja Tsho's hazard, *Hydrology and Earth System Sciences*, 22,
921 3721-3737, 10.5194/hess-22-3721-2018, 2018.
- 922 Linsbauer, A., Paul, F., Machguth, H., and Haeberli, W.: Comparing three different methods to model
923 scenarios of future glacier change in the Swiss Alps, *Annals of Glaciology*, 54, 241-253,
924 10.3189/2013AoS63A400, 2017.
- 925 Linsbauer, A., Frey, H., Haeberli, W., Machguth, H., Azam, M. F., and Allen, S.: Modelling glacier-bed
926 overdeepenings and possible future lakes for the glaciers in the Himalaya—Karakoram region, *Annals*
927 *of Glaciology*, 57, 119-130, 10.3189/2016AoS71A627, 2016.
- 928 Liu, K., Song, C., Ke, L., Jiang, L., Pan, Y., and Ma, R.: Global open-access DEM performances in Earth's
929 most rugged region High Mountain Asia: A multi-level assessment, *Geomorphology*, 338, 16-26,
930 10.1016/j.geomorph.2019.04.012, 2019.
- 931 Lützwow, N., Veh, G., and Korup, O.: A global database of historic glacier lake outburst floods, *Earth*
932 *Syst. Sci. Data Discuss.*, 2023, 1-27, 10.5194/essd-2022-449, 2023.
- 933 McClean, F., Dawson, R., and Kilsby, C.: Implications of Using Global Digital Elevation Models for
934 Flood Risk Analysis in Cities, *Water Resources Research*, 56, 10.1029/2020wr028241, 2020.
- 935 The mass flow simulation tool: <https://www.avaflow.org>, last
936 Mergili, M., Fischer, J.-T., Krenn, J., and Pudasaini, S. P.: r.avaflow v1, an advanced open-source
937 computational framework for the propagation and interaction of two-phase mass flows, *Geoscientific*
938 *Model Development*, 10, 553-569, 10.5194/gmd-10-553-2017, 2017.
- 939 Mergili, M., Jaboyedoff, M., Pullarello, J., and Pudasaini, S. P.: Back calculation of the 2017 Piz
940 Cengalo–Bondo landslide cascade with r.avaflow: what we can do and what we can learn, *Natural*
941 *Hazards and Earth System Sciences*, 20, 505-520, 10.5194/nhess-20-505-2020, 2020a.
- 942 Mergili, M., Frank, B., Fischer, J.-T., Huggel, C., and Pudasaini, S. P.: Computational experiments on the
943 1962 and 1970 landslide events at Huascarán (Peru) with r.avaflow: Lessons learned for predictive
944 mass flow simulations, *Geomorphology*, 322, 15-28, 10.1016/j.geomorph.2018.08.032, 2018a.
- 945 Mergili, M., Pudasaini, S. P., Emmer, A., Fischer, J.-T., Cochachin, A., and Frey, H.: Reconstruction of
946 the 1941 GLOF process chain at Lake Palcacocha (Cordillera Blanca, Peru), *Hydrology and Earth*
947 *System Sciences*, 24, 93-114, 10.5194/hess-24-93-2020, 2020b.
- 948 Mergili, M., Emmer, A., Juricova, A., Cochachin, A., Fischer, J. T., Huggel, C., and Pudasaini, S. P.: How
949 well can we simulate complex hydro-geomorphic process chains? The 2012 multi-lake outburst flood



- 950 in the Santa Cruz Valley (Cordillera Blanca, Peru), *Earth Surf Process Landf*, 43, 1373-1389,
951 10.1002/esp.4318, 2018b.
- 952 Muthusamy, M., Casado, M. R., Butler, D., and Leinster, P.: Understanding the effects of Digital
953 Elevation Model resolution in urban fluvial flood modelling, *Journal of Hydrology*, 596,
954 10.1016/j.jhydrol.2021.126088, 2021.
- 955 NASA-JPL: NASADEM Merged DEM Global 1 arc second V001. Distributed by OpenTopography,
956 Distributed by OpenTopography [dataset], <https://doi.org/10.5069/G93T9FD9>, 2021.
- 957 NCHM: Reassessment of Potentially Dangerous Glacial Lakes in Bhutan, National Centre for
958 Hydrology and Meteorology, Royal Government of Bhutan, National Center for Hydrology and
959 Meteorology, Royal Government of Bhutan, PO Box: 2017, Thimphu, Bhutan, 54, 2019a.
- 960 NCHM: Detailed assessment report on GLOF hazard from Thorthormi glacial lakes and associated
961 glaciers, Thimphu, 2019b.
- 962 NCHM: Action Taken Report Thorthormi Flood Incident 30th October 2023, National Center for
963 Meteorology and Hydrology, Thimphu, 17, 2023.
- 964 Nie, Y., Liu, Q., Wang, J., Zhang, Y., Sheng, Y., and Liu, S.: An inventory of historical glacial lake
965 outburst floods in the Himalayas based on remote sensing observations and geomorphological
966 analysis, *Geomorphology*, 308, 91-106, 10.1016/j.geomorph.2018.02.002, 2018.
- 967 Nie, Y., Deng, Q., Pritchard, H. D., Carrivick, J. L., Ahmed, F., Huggel, C., Liu, L., Wang, W., Lesi, M.,
968 Wang, J., Zhang, H., Zhang, B., Lü, Q., and Zhang, Y.: Glacial lake outburst floods threaten Asia's
969 infrastructure, *Science Bulletin*, 10.1016/j.scib.2023.05.035, 2023.
- 970 Obu, J., Westermann, S., Bartsch, A., Berdnikov, N., Christiansen, H. H., Dashtseren, A., Delaloye, R.,
971 Elberling, B., Etzelmüller, B., Kholodov, A., Khomutov, A., Kääh, A., Leibman, M. O., Lewkowicz, A. G.,
972 Panda, S. K., Romanovsky, V., Way, R. G., Westergaard-Nielsen, A., Wu, T., Yamkhin, J., and Zou, D.:
973 Northern Hemisphere permafrost map based on TTOP modelling for 2000–2016 at 1 km² scale,
974 *Earth-Science Reviews*, 193, 299-316, 10.1016/j.earscirev.2019.04.023, 2019.
- 975 Pudasaini, S. P.: A general two-phase debris flow model, *Journal of Geophysical Research: Earth
976 Surface*, 117, 10.1029/2011jf002186, 2012.
- 977 Pudasaini, S. P. and Krautblatter, M.: A two-phase mechanical model for rock-ice avalanches, *Journal
978 of Geophysical Research: Earth Surface*, 119, 2272-2290, 10.1002/2014jf003183, 2014a.
- 979 Pudasaini, S. P. and Krautblatter, M.: A two-phase mechanical model for rock-ice avalanches, *Journal
980 of Geophysical Research: Earth Surface*, 119, 2272-2290, 10.1002/2014jf003183, 2014b.
- 981 Pudasaini, S. P. and Mergili, M.: A Multi-Phase Mass Flow Model, *Journal of Geophysical Research:
982 Earth Surface*, 124, 2920-2942, 10.1029/2019jf005204, 2019.
- 983 Rinzin, S., Zhang, G., and Wangchuk, S.: Glacial Lake Area Change and Potential Outburst Flood
984 Hazard Assessment in the Bhutan Himalaya, *Frontiers in Earth Science*, 9,
985 10.3389/feart.2021.775195, 2021.
- 986 Rinzin, S., Zhang, G., Sattar, A., Wangchuk, S., Allen, S. K., Dunning, S., and Peng, M.: GLOF hazard,
987 exposure, vulnerability, and risk assessment of potentially dangerous glacial lakes in the Bhutan
988 Himalaya, *Journal of Hydrology*, 619, 10.1016/j.jhydrol.2023.129311, 2023.
- 989 Rounce, D., Watson, C., and McKinney, D.: Identification of Hazard and Risk for Glacial Lakes in the
990 Nepal Himalaya Using Satellite Imagery from 2000–2015, *Remote Sens-Basel*, 9, 10.3390/rs9070654,
991 2017.
- 992 Rounce, D. R., McKinney, D. C., Lala, J. M., Byers, A. C., and Watson, C. S.: A new remote hazard and
993 risk assessment framework for glacial lakes in the Nepal Himalaya, *Hydrology and Earth System
994 Sciences*, 20, 3455-3475, 10.5194/hess-20-3455-2016, 2016.
- 995 Saksena, S. and Merwade, V.: Incorporating the effect of DEM resolution and accuracy for improved
996 flood inundation mapping, *Journal of Hydrology*, 530, 180-194, 10.1016/j.jhydrol.2015.09.069, 2015.
- 997 Saltelli, A., Tarantola, S., Campolongo, F., and Ratto, M.: Sensitivity analysis in practice: a guide to
998 assessing scientific models, Wiley Online Library 2004.



- 999 Sattar, A., Haritashya, U. K., Kargel, J. S., Leonard, G. J., Shugar, D. H., and Chase, D. V.: Modeling lake
1000 outburst and downstream hazard assessment of the Lower Barun Glacial Lake, Nepal Himalaya,
1001 *Journal of Hydrology*, 598, 10.1016/j.jhydrol.2021.126208, 2021a.
- 1002 Sattar, A., Goswami, A., Kulkarni, A. V., Emmer, A., Haritashya, U. K., Allen, S., Frey, H., and Huggel, C.:
1003 Future Glacial Lake Outburst Flood (GLOF) hazard of the South Lhonak Lake, Sikkim Himalaya,
1004 *Geomorphology*, 388, 10.1016/j.geomorph.2021.107783, 2021b.
- 1005 Sattar, A., Allen, S., Mergili, M., Haeberli, W., Frey, H., Kulkarni, A. V., Haritashya, U. K., Huggel, C.,
1006 Goswami, A., and Ramsankaran, R.: Modeling Potential Glacial Lake Outburst Flood Process Chains
1007 and Effects From Artificial Lake-Level Lowering at Gepang Gath Lake, Indian Himalaya, *Journal of*
1008 *Geophysical Research: Earth Surface*, 128, 10.1029/2022jf006826, 2023.
- 1009 Schneider, D., Huggel, C., Cochachin, A., Guillén, S., and García, J.: Mapping hazards from glacier lake
1010 outburst floods based on modelling of process cascades at Lake 513, Carhuaz, Peru, *Advances in*
1011 *Geosciences*, 35, 145-155, 10.5194/adgeo-35-145-2014, 2014.
- 1012 Schumann, G. J. P. and Bates, P. D.: The Need for a High-Accuracy, Open-Access Global DEM, *Frontiers*
1013 *in Earth Science*, 6, 10.3389/feart.2018.00225, 2018.
- 1014 Shean, D.: High Mountain Asia 8-meter DEM mosaics derived from optical imagery, version 1,
1015 Boulder, CO: NASA National Snow and Ice Data Center Distributed Active Archive Center. doi, 10,
1016 002214309790152555, 2017a.
- 1017 Shean, D.: High Mountain Asia 8-meter DEM mosaics derived from optical imagery (1), NASA
1018 National Snow and Ice Data Center Distributed Active Archive Center [dataset], 2017b.
- 1019 Shean, D. E., Alexandrov, O., Moratto, Z. M., Smith, B. E., Joughin, I. R., Porter, C., and Morin, P.: An
1020 automated, open-source pipeline for mass production of digital elevation models (DEMs) from very-
1021 high-resolution commercial stereo satellite imagery, *ISPRS Journal of Photogrammetry and Remote*
1022 *Sensing*, 116, 101-117, 10.1016/j.isprsjprs.2016.03.012, 2016.
- 1023 Shrestha, F., Steiner, J. F., Shrestha, R., Dhungel, Y., Joshi, S. P., Inglis, S., Ashraf, A., Wali, S., Walizada,
1024 K. M., and Zhang, T.: HMAGLOFDB v1.0 – a comprehensive and version controlled database of glacier
1025 lake outburst floods in high mountain Asia, *Earth Syst. Sci. Data Discuss.*, 2023, 1-28, 10.5194/essd-
1026 2022-395, 2023.
- 1027 Shugar, D. H., Burr, A., Haritashya, U. K., Kargel, J. S., Watson, C. S., Kennedy, M. C., Bevington, A. R.,
1028 Betts, R. A., Harrison, S., and Strattman, K.: Rapid worldwide growth of glacial lakes since 1990,
1029 *Nature Climate Change*, 10, 939-945, 10.1038/s41558-020-0855-4, 2020.
- 1030 Shugar, D. H., Jacquemart, M., Shean, D., Bhushan, S., Upadhyay, K., Sattar, A., Schwanghart, W.,
1031 McBride, S., de Vries, M. V. W., Mergili, M., Emmer, A., Deschamps-Berger, C., McDonnell, M.,
1032 Bhambri, R., Allen, S., Berthier, E., Carrivick, J. L., Clague, J. J., Dokukin, M., Dunning, S. A., Frey, H.,
1033 Gascoin, S., Haritashya, U. K., Huggel, C., Kääb, A., Kargel, J. S., Kavanaugh, J. L., Lacroix, P., Petley, D.,
1034 Rupper, S., Azam, M. F., Cook, S. J., Dimri, A. P., Eriksson, M., Farinotti, D., Fiddes, J., Gnyawali, K. R.,
1035 Harrison, S., Jha, M., Koppes, M., Kumar, A., Leinss, S., Majeed, U., Mal, S., Muhuri, A., Noetzli, J.,
1036 Paul, F., Rashid, I., Sain, K., Steiner, J., Ugalde, F., Watson, C. S., and Westoby, M. J.: A massive rock
1037 and ice avalanche caused the 2021 disaster at Chamoli, Indian Himalaya, *Science*, 373, 300,
1038 10.1126/science.abh4455, 2021.
- 1039 Somos-Valenzuela, M. A., McKinney, D. C., Byers, A. C., Rounce, D. R., Portocarrero, C., and Lamsal,
1040 D.: Assessing downstream flood impacts due to a potential GLOF from Imja Tsho in Nepal, *Hydrology*
1041 *and Earth System Sciences*, 19, 1401-1412, 10.5194/hess-19-1401-2015, 2015.
- 1042 Taylor, C., Robinson, T. R., Dunning, S., Rachel Carr, J., and Westoby, M.: Glacial lake outburst floods
1043 threaten millions globally, *Nature Communications*, 14, 487, 10.1038/s41467-023-36033-x, 2023.
- 1044 Thompson, I., Shrestha, M., Chhetri, N., and Agusdinata, D. B.: An institutional analysis of glacial
1045 floods and disaster risk management in the Nepal Himalaya, *International Journal of Disaster Risk*
1046 *Reduction*, 47, 10.1016/j.ijdr.2020.101567, 2020.
- 1047 Uemaa, E., Ahi, S., Montibeller, B., Muru, M., and Kmoch, A.: Vertical Accuracy of Freely Available
1048 Global Digital Elevation Models (ASTER, AW3D30, MERIT, TanDEM-X, SRTM, and NASADEM), *Remote*
1049 *Sens-Basel*, 12, 10.3390/rs12213482, 2020.



- 1050 Veh, G., Lützow, N., Kharlamova, V., Petrakov, D., Hugonnet, R., and Korup, O.: Trends, Breaks, and
1051 Biases in the Frequency of Reported Glacier Lake Outburst Floods, *Earth's Future*, 10,
1052 10.1029/2021ef002426, 2022.
- 1053 Veh, G., Lutzow, N., Tamm, J., Luna, L. V., Hugonnet, R., Vogel, K., Geertsema, M., Clague, J. J., and
1054 Korup, O.: Less extreme and earlier outbursts of ice-dammed lakes since 1900, *Nature*,
1055 10.1038/s41586-022-05642-9, 2023.
- 1056 Vilca, O., Mergili, M., Emmer, A., Frey, H., and Huggel, C.: The 2020 glacial lake outburst flood process
1057 chain at Lake Salkantaycocha (Cordillera Vilcabamba, Peru), *Landslides*, 18, 2211-2223,
1058 10.1007/s10346-021-01670-0, 2021.
- 1059 Wang, W., Yang, X., and Yao, T.: Evaluation of ASTER GDEM and SRTM and their suitability in hydraulic
1060 modelling of a glacial lake outburst flood in southeast Tibet, *Hydrological Processes*, 26, 213-225,
1061 10.1002/hyp.8127, 2011.
- 1062 Wang, X., Guo, X., Yang, C., Liu, Q., Wei, J., Zhang, Y., Liu, S., Zhang, Y., Jiang, Z., and Tang, Z.: Glacial
1063 lake inventory of high-mountain Asia in 1990 and 2018 derived from Landsat images, *Earth System
1064 Science Data*, 12, 2169-2182, 10.5194/essd-12-2169-2020, 2020.
- 1065 Wang, Y., Hutter, K., and Pudasaini, S. P.: The Savage-Hutter theory: A system of partial differential
1066 equations for avalanche flows of snow, debris, and mud, *ZAMM - Journal of Applied Mathematics
1067 and Mechanics / Zeitschrift für Angewandte Mathematik und Mechanik*, 84, 507-527,
1068 10.1002/zamm.200310123, 2004.
- 1069 Westoby, M. J., Glasser, N. F., Brasington, J., Hambrey, M. J., Quincey, D. J., and Reynolds, J. M.:
1070 Modelling outburst floods from moraine-dammed glacial lakes, *Earth-Science Reviews*, 134, 137-159,
1071 10.1016/j.earscirev.2014.03.009, 2014.
- 1072 Westoby, M. J., Brasington, J., Glasser, N. F., Hambrey, M. J., Reynolds, J. M., Hassan, M. A. A. M., and
1073 Lowe, A.: Numerical modelling of glacial lake outburst floods using physically based dam-breach
1074 models, *Earth Surface Dynamics*, 3, 171-199, 10.5194/esurf-3-171-2015, 2015.
- 1075 Worni, R., Huggel, C., and Stoffel, M.: Glacial lakes in the Indian Himalayas--from an area-wide glacial
1076 lake inventory to on-site and modeling based risk assessment of critical glacial lakes, *Sci Total
1077 Environ*, 468-469 Suppl, S71-84, 10.1016/j.scitotenv.2012.11.043, 2013.
- 1078 Worni, R., Stoffel, M., Huggel, C., Volz, C., Casteller, A., and Luckman, B.: Analysis and dynamic
1079 modeling of a moraine failure and glacier lake outburst flood at Ventisquero Negro, Patagonian
1080 Andes (Argentina), *Journal of Hydrology*, 444-445, 134-145, 10.1016/j.jhydrol.2012.04.013, 2012.
- 1081 Zhang, G., Yao, T., Xie, H., Wang, W., and Yang, W.: An inventory of glacial lakes in the Third Pole
1082 region and their changes in response to global warming, *Global and Planetary Change*, 131, 148-157,
1083 10.1016/j.gloplacha.2015.05.013, 2015.
- 1084 Zhang, G., Bolch, T., Yao, T., Rounce, D. R., Chen, W., Veh, G., King, O., Allen, S. K., Wang, M., and
1085 Wang, W.: Underestimated mass loss from lake-terminating glaciers in the greater Himalaya, *Nature
1086 Geoscience*, 10.1038/s41561-023-01150-1, 2023a.
- 1087 Zhang, T., Wang, W., An, B., and Wei, L.: Enhanced glacial lake activity threatens numerous
1088 communities and infrastructure in the Third Pole, *Nature Communications*, 14, 10.1038/s41467-023-
1089 44123-z, 2023b.
- 1090 Zheng, G., Mergili, M., Emmer, A., Allen, S., Bao, A., Guo, H., and Stoffel, M.: The 2020 glacial lake
1091 outburst flood at Jinwuco, Tibet: causes, impacts, and implications for hazard and risk assessment,
1092 *The Cryosphere Discuss.*, 2021, 1-28, 10.5194/tc-2020-379, 2021a.
- 1093 Zheng, G., Allen, S. K., Bao, A., Ballesteros-Cánovas, J. A., Huss, M., Zhang, G., Li, J., Yuan, Y., Jiang, L.,
1094 Yu, T., Chen, W., and Stoffel, M.: Increasing risk of glacial lake outburst floods from future Third Pole
1095 deglaciation, *Nature Climate Change*, 11, 411-417, 10.1038/s41558-021-01028-3, 2021b.

1096